Multiphysics Computational Modeling of Implantable Actuable Devices for Local Epicardial Therapy Delivery

by

Yiling Fan

Submitted to the Department of Mechanical Engineering
in partial fulfillment of the requirements for the degree of

Master of Science in Mechanical Engineering

at the

MASSACHUSETTS INSTITUTE OF TECHNOLOGY

June 2019

Author ..... Signature redacted .....
Department of Mechanical Engineering
May 20, 2019

Certified by..... Signature redacted .....
Ellen Roche
Assistant Professor
Thesis Supervisor

Signature redacted

Accepted by .....
Nicolas Hadjiconstantinou
Chairman, Department Committee on Graduate Theses

Multiphysics Computational Modeling of Implantable Actuable Devices for Local Epicardial Therapy Delivery

by

Yiling Fan

Submitted to the Department of Mechanical Engineering
on May 20, 2019, in partial fulfillment of the
requirements for the degree of
Master of Science in Mechanical Engineering

Abstract

Over the past few decades, heart disease remainis the leading cause of death globally. Local myocardial delivery of cardiac therapies is a potential method to improve the efficiency and expand the variety of cardiac therapies due to its capability of providing high local concentrations with minimal systemic exposure. Recently, our group has developed two epicardial (outer wall of the heart) delivery devices, called "Therepi" and "fibRobot", that are implantable, replenishable and actuatable. They have the potential to improve the efficiency of drug delivery by enabling the capability of giving multiple dose of therapies with only one implantation surgery and reducing the foreign body responses through mechanical oscillation. In this thesis, we used different computational models (structural, drug diffusion, and fluid-structure interaction) to characterize the therapeutic effect of these two devices on the heart. We also used the validated computational models to evaluate iterative designs of each device and purpose an optimization work-flow for these devices. The drug transport model showed anisotropic diffusion in the myocardium with increasing diffusivity along fiber orientation. Transmural penetration was slow in the model, taking over 5 days to diffuse through the left ventricular wall. Various design evaluations showed that the transmural penetration speed can be improved by increasing the area of the reservoir-epicardium interface. Seperately, in a the structural model, we showed that "fibRobot" can provide 7% of strain on to its lower membrane during actuation. The model also showed that, if higher strain is required in order to modulate the foreign body response, we will need to either increase the actuation pressure, increase the membrane radius, reduce the membrane thickness, or reduce the membrane stiffness. In the future, we plan to couple these models to a multiphysics model to thoroughly characterize the drug transport from our epicardial device to the heart.

Thesis Supervisor: Ellen Roche
Title: Assistant Professor

Acknowledgments

I would like to thank all the people that have helped and supported me throughout my Master's journey. First of all, I would like to thank my advisor, Professor Ellen Roche, who has given me numerous support and is always trying to encourage me while I am finding my path in field of science and engineering.

I also want to thank Dr. William Ronan from the National Univeristy of Ireland Galway for giving advise on the diffusion modeling. I would like acknowledge Dr. Christopher Nguyen from Massachusetts General Hospital who helped to collect the diffusion imaging and provided the left ventricle DTI data.

I also want to thank all my colleagues from the MIT TTDD Lab who are inspiring and always willing to offer helps. It is a great pleasure to work with all of you.

Last but know least, I want to thank my friends and family from China. I would not be able to accomplish all the work in this thesis without their loves and support.

Contents

List of Figures

List of Tables

Chapter 1

Introduction

Cardiovascular disease (CVD) is a group of disorders associated with the heart and blood vessels. Although various cardiovascular therapies have made tremendous impact on reducing the morbidity and mortality of CVD over the past few decades, it is still the leading cause of death globally, causing over 17.5 million, or approximately 31%, of all deaths worldwide [1]. Among CVD, heart disease is the primary pathology (over 50%), causing over 630,000 deaths in America in 2016 [2]. Local myocardial delivery (LMD) is a promising method to improve many different kinds of cardiac therapies by reducing the systemic administration barriers and increasing concentration of drug on target regions. Over the past few decades, researchers have developed various methods for local myocardial delivery, ranging from attaching drug-loaded polymeric patches on the epicardium by open heart surgery [3] to extruding hydrogel to the pericardium through a minimally invasive catheter [4] and injecting therapies to the pericardial space through a minimally invasive robot [5].

Recently, our group has developed two devices for epicardial drug delivery, the "Therepi" [6] and the "fibRobot" [7]. "Therepi" is a replenishable implanted epicardial reservoir that can delivery multiscale cardiac therapies (drugs, growth factors, and cells) to the heart via passive diffusion. Our study demonstrated functional benefit in various cardiac indexes after multiple deliveries of mesenchymal stem cells to the epicardium through the Therepi system. "fibRobot" is a related device that can actively deliver therapies by means of pneumatic actuation. In addition, when

actuated daily at low frequencies (1 Hz) for 5 minutes, the device is found to have benefit for modulating foreign body response around the device-tissue interface. We hypothesize that the benefit results from the mechanical oscillation which modulates the biomechanics of the biotic-abiotic interface by perturbing fluid flow and cellular activity in the peri-implant tissue and therefore interferes with the progression of the foreign body responses [7].

In this thesis, I try to use computational modeling techniques to understand the mechanisms behind the observed functional benefits of the *in vivo* studies and therefore guide the design optimization of these devices. The aims of this study are to:

1. Use diffusion tensor magnetic resonance imaging (DT-MRI or DTI) to track the dynamic process of drug diffusion in the myocardium and use finite element analysis (FEA) to characterize this diffusion process.

2. Use the validated FEA diffusion model to propose enhanced designs of the Therepi.

3. Use FEA to characterize the mechanical effect of the fibRobot on the biotic-abiotic interface.

4. Couple the structural model (FEA) with a fluid model (smooth particle hydrodynamics) to study the surrounding fluid flow effect resulting from the fibRobot.

An overview diagram of this thesis is shown in Fig. 1-1. In Chapter 2, I will review a number of major heart diseases and their current treatments; current development of epicardial drug delivery; the diffusion tensor imaging (DTI) technique, as well as different studies of computational modeling of cardiac devices. In Chapter 3, the anisotropic diffusion in the myocardium will be characterized and used to study drug distribution of various Therepi designs on a subject-specific left ventricle finite element model. In Chapter 4, the fibRobot will be modeled using both structural and fluid-structural interaction analyses to investigate the mechanical effect of the actuation on the biotic-abiotic interface. In Chapter 5, the future work of connecting

these two works and coupling the three physical processes in this type of epicardial drug delivery will be discussed.

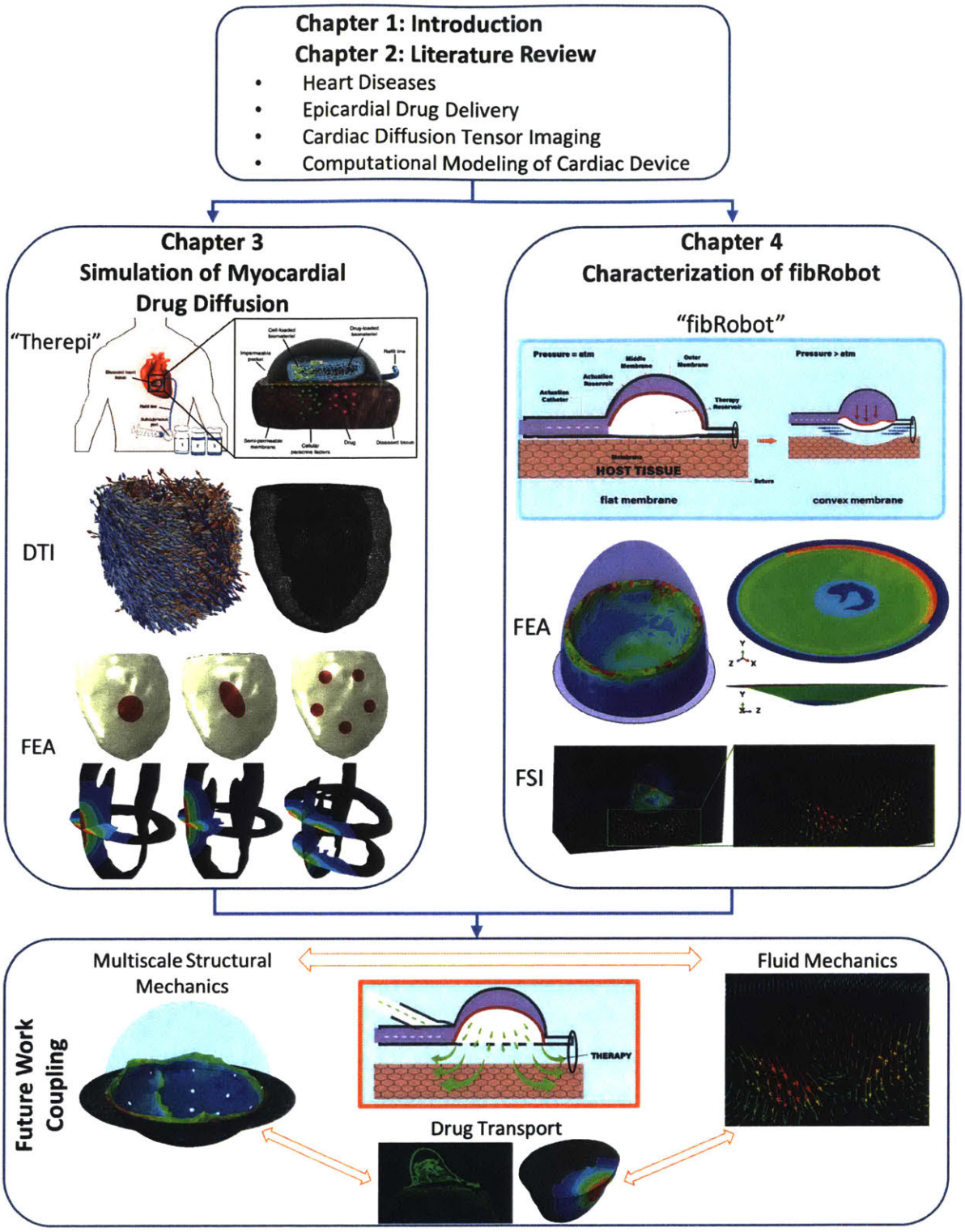

Figure 1-1: Thesis Overview. DTI = diffusion tensor imaging; FEA = finite element analysis; FSI = fluid-structure interaction

Chapter 2

Literature Review

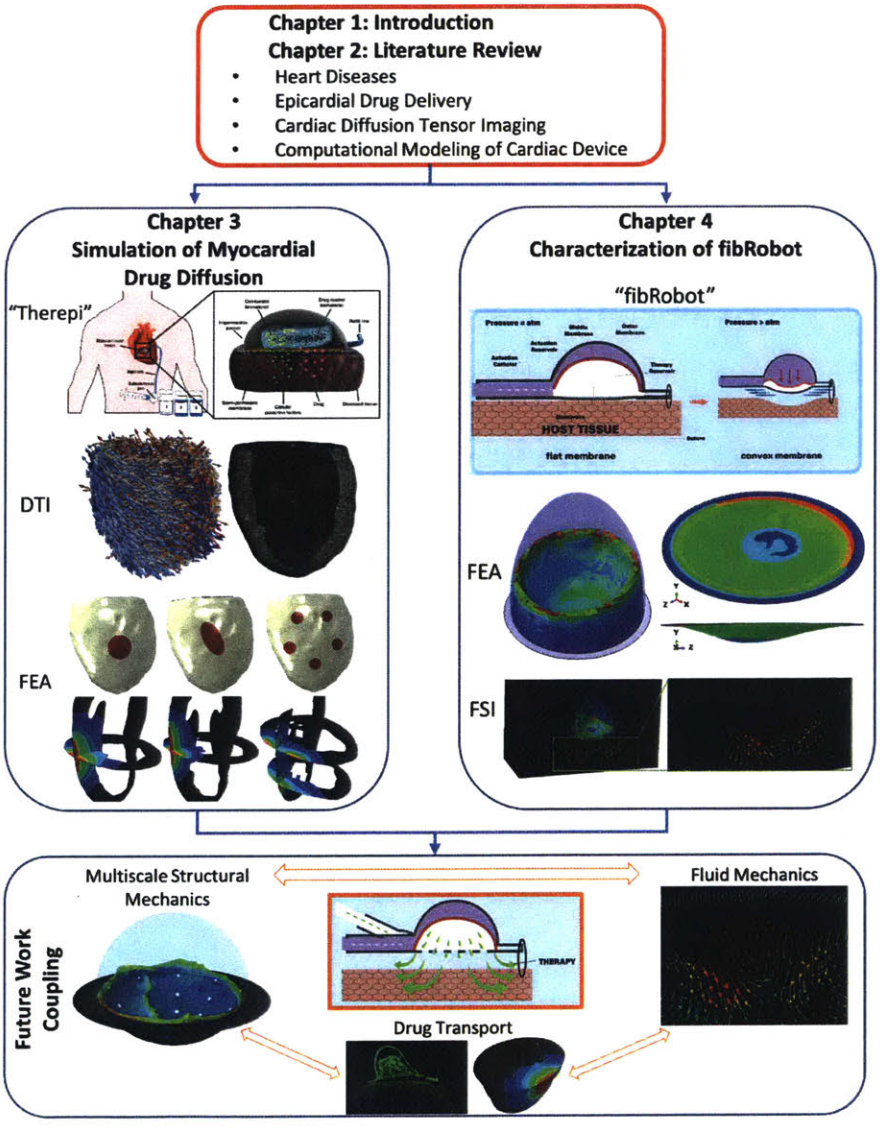

2.1 Heart Disease

Over the past three decades, heart disease reminds the leading cause of death in the United States, causing over 630,000 deaths in the United States in 2016 [2]. Common heart diseases are coronary artery disease (CAD), arrhythmia, heart valve disease, heart muscle disease (also known as cardiomyopathy), congenital heart disease, and heart failure (which can be caused by any of these conditions). Various drugs have been developed to act as effective therapies for different kinds of heart diseases. For example, Amiodarone is widely used to treat arrythmia; Angiotensin-converting enzyme inhibitors, angiotensin II receptor blockers and Beta blockers can reduce blood pressure for CAD and cardiomyopathy. Other drugs, such as Diuretics (to reduce ventricular preload), Aspirin (for blood-thinning), and Digoxin (to increase contraction) are also widely used to reduce the symptoms of heart failure. Other heart diseases that are congenital or related to heart valves and structural heart diseases normally require surgical intervention. However, post-surgery complications usually need to be controlled with therapeutic treatments. Therefore, cardiovascular drugs play an important role in reducing morbidity and mortality of heart diseases.

2.2 Local Myocardial Drug Delivery

Although various of drugs have been developed for cardiovascular diseases, they are only effective when they are bounded/concentrated to the corresponding target regions. Systemic administration impairs the effectiveness of these drugs significantly due to systemic clearance, and off-target toxicities. Local myocardial delivery (LMD), where drug is delivered directly to theart muscle, is a promising method to enhance clinical benefit of these drugs. LMD methods can be classified into four categories: (1) intrapericardial (IPC) delivery, (2) epicardial (EC) delivery, (3) intramyocardial (IMC) delivery, and (4) intracoronary (IC) delivery [8].

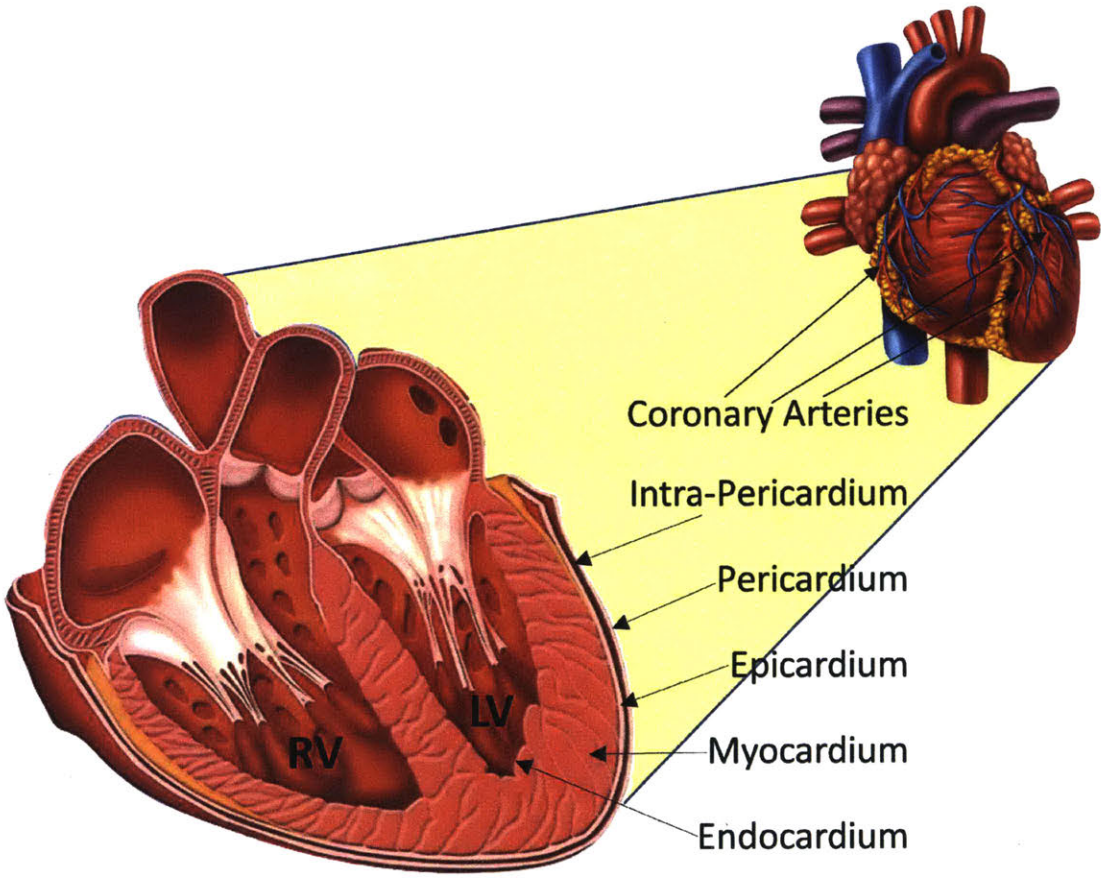

Figure 2-1: Heart anatomy. LV = left ventricle; RV = right ventricle.

Here we focus on epicardial delivery and will summarize the types of therapy, delivery devices and outcomes in different EC delivery studies. Over the past three

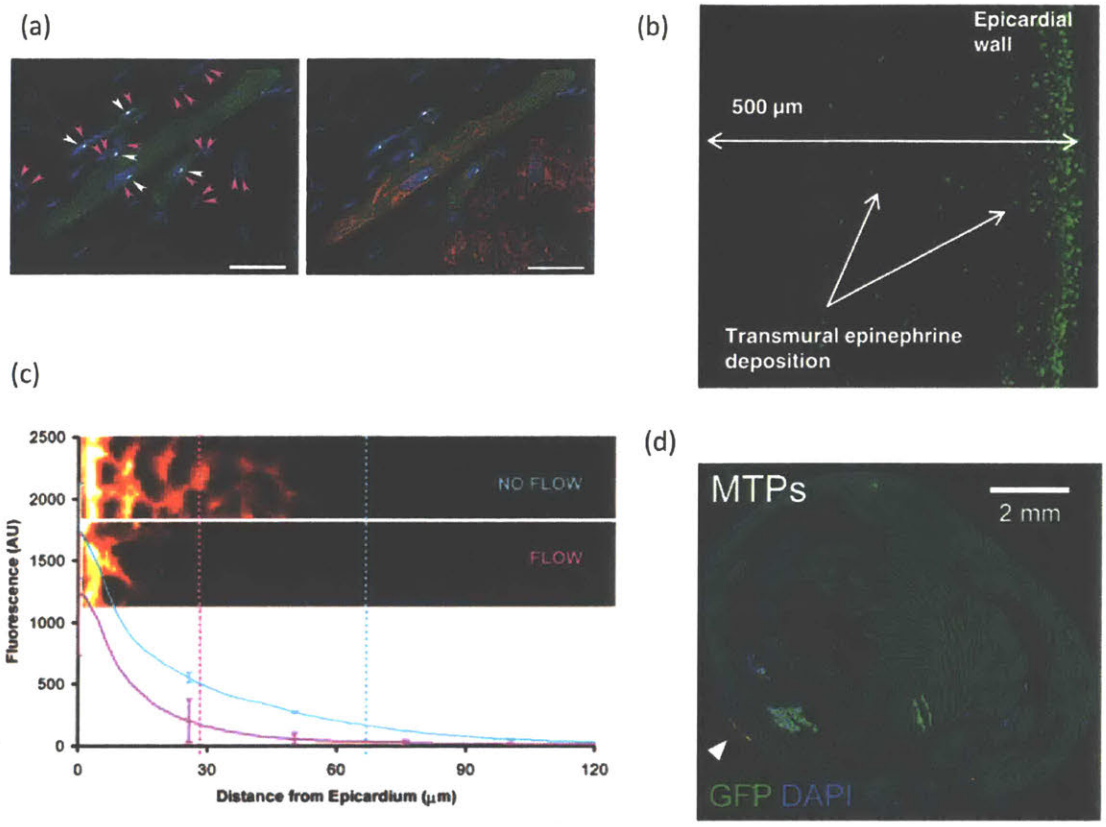

Figure 2-2: Different quantification techniques for drug distribution assessment. (a) Fluorescence in situ hybridization (FISH) analysis showing newly formed cardiomyocytes (desmin, red) [9]. (b) Immunohistochemical microscopy shows the transmural distribution of epinephrine bound to adrenergic receptors after EC delivery [3]. (c) Fluorescence microscopy images of the growth factor (Texas Red–FGF2) distribution in rat myocardium [10]. (d) Ex vivo stained for GFP (green) with DAPI (blue) nuclear stain on a rat heart showing the intramyocardial graft (arrow head) [11].

decades, studies have tried to use EC delivery to administrate different therapies to the heart, from anti-arrhythmic [12, 13, 14, 15] and inotropic [3, 16] drugs to growth factors [17, 10] and stem cells [9, 11]. Besides looking at the indices of cardiac function, most studies with drug administration [12, 13, 14, 15] use high-performance liquid chromatography (HPLC) to quantify the content of drug in different regions of the myocardium. More recently, immunostaining has been used to show the transmural distribution of the drug in the myocardial wall [3], especially for studies involving growth factors or stem cells [10, 11], see Fig. 2-2. Other methods such as growth

factor radioactivity quantification [10] and *in vivo* MRI tissue analysis [17] have also been explored to assess the performance of EC delivery. Regarding the vehicles for EC delivery, most of these studies used polyurethene-based or alginate-based polymeric patches as the drug reservoirs for releasing the therapies. A more advanced device, Osmotic Minipumps (Model 2ML4, Alzet Pharmaceuticals), was used by Pearlman et al. [17] to deliver growth factors in a more controlled manner. Stem cells were delivered directly via tissue cultured cell sheets. More recently, more sophisticated EC delivery devices have been developed in which the drug reservoir can easily be replenished and/or only require minimally invasive surgery, see Fig. 2-3(d-f).

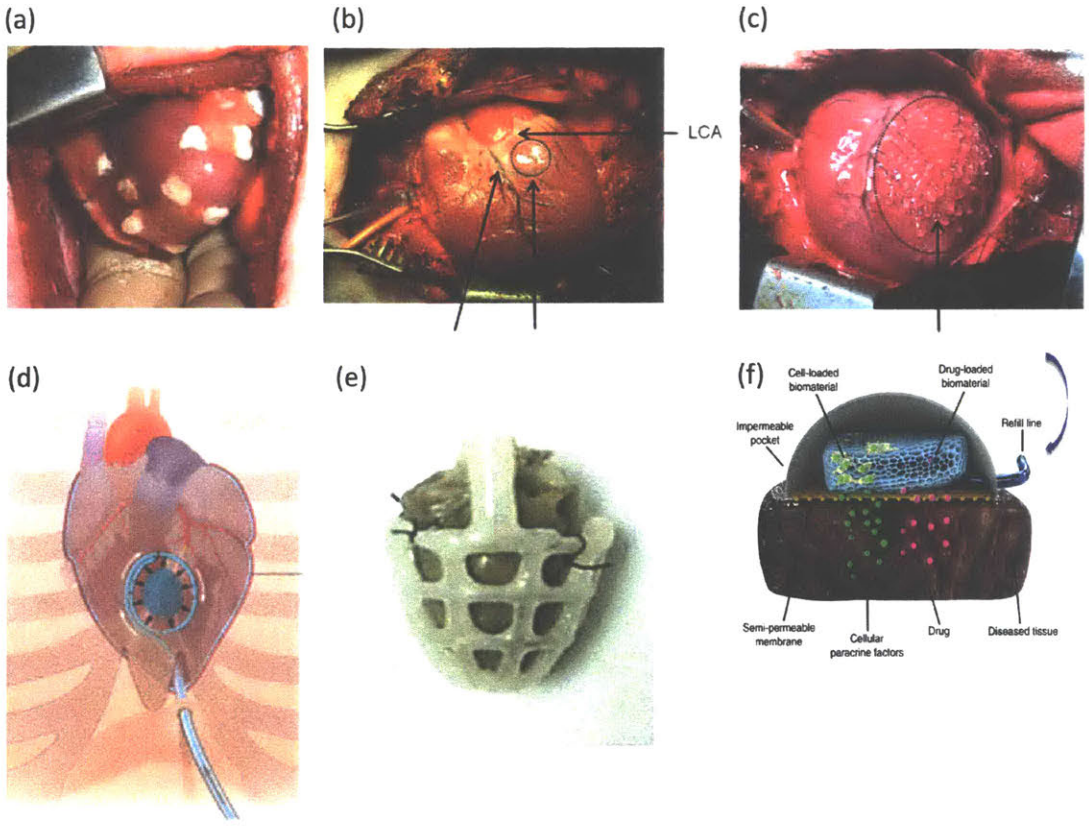

Figure 2-3: Pericardial or epicardial delivery devices. EC delivery via (a) gelfoam [18], (b) alginate disk [3], and (c) poloxamer [3]. (d) Minimally invasive device for epicardial hydrogel delivery [4]. (e) An implantable EC delivery device [19]. (f) "Therepi", an replenishable implantable EC delivery device [20].

Table 2.1: Epicardial Drug Delivery. (HPLC = high-performance liquid chromatography; hESC = human embryonic stem cell

Study	Therapy	Delivery Method	Drug Distribution Assessment
Siden, 1992 [14]	Propranolol	Polyurethane-silicone patch	HPLC
Labhasetwar, 1993 [12]	Sotalol	Polyurethane patch	HPLC
Labhasetwar, 1994 [13]	Sotalol	Polyurethane patch	HPLC
Bolderman, 2011 [15]	Amiodarone	Polyethylene glycol-based hydrogel	HPLC
Maslov, 2013 [16]	Epinephrine	Alginate disk	• Epinephrine tissue concentration • Upregulation of cAMP
Maslov, 2014 [3]	Epinephrine	Alginate disk or poloxamer	Immunostaining
Pearlman, 1995 [17]	Growth factor (VEGF)	Osmotic minipumps	*(MRI tissue evaluation)
Le, 2009 [10]	Growth factor	Sodium alginate polymeric device	• Epifluorescence imaging • Radioactivity quantification
Gerbine, 2015 [11]	hESC	hESC-cardiac tissue patches	Fluorescent imaging
Miyahara, 2006 [9]	Mesenchymal stem cells	Cell sheet	Fluorescence *in situ* hybridization (FISH)

2.3 Diffusion Tensor Imaging

2.3.1 Basic physics of magnetic resonance imaging (MRI)

Magnetic resonance imaging (MRI) is based on the magnetic properties of hydrogen atoms to generate images of the anatomy. The hydrogen atoms are first aligned by the strong primary magnetic field. Then radial frequency (RF) is applied by the RF coils to interfere the alignment. The atoms return to their resting alignment through various relaxation processes. During these processes, the atoms emit RF signals which are measured by the RF coils and converted to different pixel intensities in order to form pictures. The two relaxation processes are T1 and T2, which are the relaxation modes in the longitudinal and transverse axes, respectively. More specifically, T1 is the time it takes for the spinning atoms to realign with the primary magnetic field after the RF pulse. T2 is the time it takes for the spinning atoms to lose phrase coherence in the transverse axis after RF pulse. To identify different types of tissue, different types of images can be generated by applying different sequences of RF pulses. The two most common types of images are T1-weighted and T2-weighted images where the pixel intensity is predominately determine by T1 relaxation in the former sequence and the by T1 relaxation in the latter sequence.

2.3.2 Basic physics of diffusion tensor MRI

Diffusion tensor magnetic resonance imaging (DT-MRI or DTI) [21] is an imaging technique that can detect the anisotropic diffusion of water in tissue. Therefore, it can be used as a non-destructive method to reveal the microstructure and tissue architecture, more specifically the fiber structure.

Diffusion imaging is based on the theory that water molecules have restricted (anisotropic) diffusion inside the fiber instead of free (isotropic) diffusion which follows the normal Brownian motion. Due to the tubular structure of the fiber, the water molecules inside preferentially move along the fiber axis. By applying two identical but opposite magnetic gradients sequentially to shift and reverse the spinning phase of

the proton, it is able to detect restriction diffusion in the gradient direction comparing the signal intensity of the diffusion imaging to the baseline T2 weighted image. In order to fully characterize diffusion in 3D space, we need a 3×3 tensor representing the diffusion tensity in 9 directions, see below. By assuming the diffusion is transversely isotropic, meaning the diffusion restriction in the plane perpendicular to the fiber axis is isotropic, the tensor becomes symmetric and have only 6 independent components (xx, xy, xz, yy, yz, zz). Thus, diffusion tensor imaging applies diffusion gradients in the 6 directions of each voxel to get a 3×3 symmetric matrix. The primary eigenvector of the matrix represent the fast diffusion direction. It has been shown in a cardiac-DTI study that the primary and secondary eigenvectos align with the fiber and sheetlet normal directions of the myocardium, respectively [22]. An example of cardiac-DTI data and the different fiber structure directions are illustrated in Fig. 2-4.

$$\begin{bmatrix} xx & xy & xz \\ yx & yy & yz \\ zx & zy & zz \end{bmatrix}$$

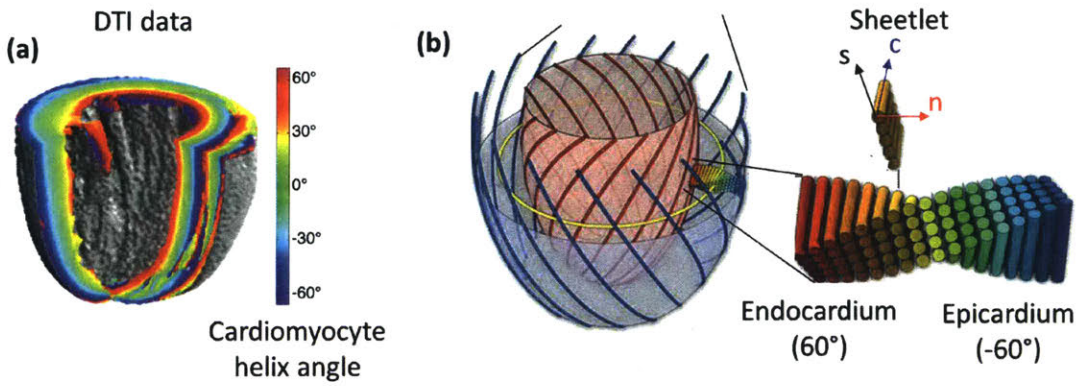

Figure 2-4: Cardiac diffusion tensor imaging. (a) Cardiomyocyte helix angle across the ventricular wall (adapted with permission from [23]). (b) Demonstration of cardiomyocyte orientation and sheetlet orientation in the LV (adapted with permission from [24]). c = fiber, s = sheetlet, n = sheetlet-normal.

2.4 Computational Modeling for Cardiac Therapies

In recent years, computational modeling has been used to assist the design and development of a wide range of medical devices. In fact, the Food and Drug Administration (FDA) provides guidance on how to report the computational modeling studies of medical devices [25]. The field of cardiac medical devices, in particular, has adopted various traditional computational modeling techniques including solid mechanics (e.g. stent fatigue assessment [26]), fluid mechanics (e.g. evaluation of blood flow after transcatheter aortic valve replacement [27]), and thermal propagation (e.g. evaluation of heat dissipation in ventricular assist devices [28]). More advanced models have used the fluid-structure interaction method to simulate transcatheter aortic valve placement [29] and the electrophysiology of the heart to guide arrhythmia ablation [30].

Simulations of drug release in the cardiovascular system are much less studied. Since local myocardial delivery is relative new, to our knowledge, there is no previous study modeling the transport of drug in the myocardium. The majority of previous studies examined drug release in the vessels because of the prevalence of drug eluting stent in the past decade. Hose et al. [31] used a thermal analogy to simulate diffusion and advection of drug releasing from stents to vessels. Migliavacca et al. [32] and Horner et al. [33] used the same analogy in their models and included drug binding to one or more specific receptors in the arterial wall. A more recent study further improved the model by considering non-specific binding due to the trapping of drug in the extracellular matrix [34]. In addition, Zunino et al. [35] coupled the drug release model in the arterial wall with the fluid dynamics model in the arterial lumen in order to account for the contribution of drug releasing into the blood flow. Similar advection-diffusion model have been used to study drug delivery in the trabecular bone [36] and in the dermal layers [37].

Computational modeling, and the finite element (FE) method in particular, has been widely used to study other mechanical devices for cardiac therapy. Jhun et al. [38] created a simplified LV model to show that increasing passive epicardial con-

straint effectively eliminated end-diastolic myofiber stress but also reduced ejection fraction. The biventricular FE model investigating the Acorn CorCap Cardiac Support Device (CSD) also showed similar results [39]. The endocardial patch used in the Dor procedure has been studied by Sun et al.[40] and Pantoja et al. [41] showing that the Dor procedure can attenuate myofiber stress. The latter study also found that the procedure induced residual stress in the border zone (compression) and the remote region (tension).

FEA was also used to study more sophisticated ventricular restraint devices. Carrick et al. [42] showed the mechanical benefit of the Coaspsys, an epicardial restraint device for mitral regurgitation, in their patient-specific model. More recently, the FE model created by Park et al. [43] showed the mechanical effect of cardioplasty wraps on a rat heart. They showed that a full film wrap significantly reduced the ventricular compliance resulting in an elevated end-diastolic pressure and decreased end-diastolic volume while the mesh wrap only slightly altered the mechanical properties comparing to the baseline. Sack et al. [44] used the four-chamber human heart model to demonstrate the benefits of left ventricular assist device (LVAD) on left ventricle (LV) stress reduction. However, the simulation predicted a less substantial effect on right ventricle (RV) stress reduction which indicates a potential direction for VAD improvement.

Chapter 3

Simulation of Drug Diffusion in Myocardial Tissue

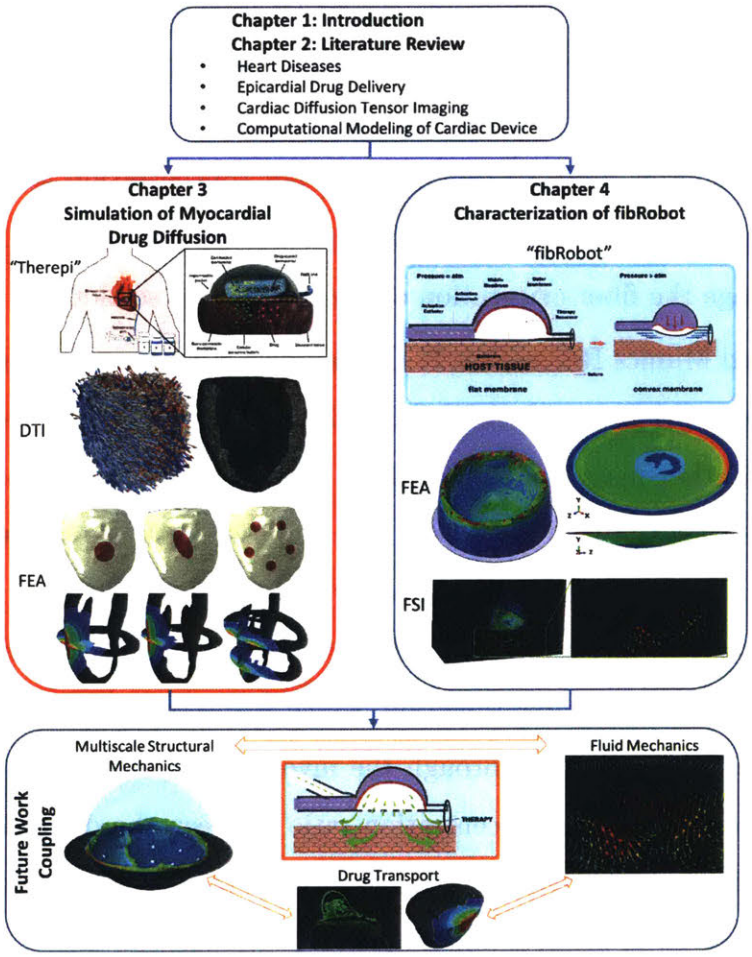

3.1 Method

In order to characterize the diffusion properties of myocardium, we diffused gadoterate meglumine (Dotarem), a Gadolinium-based MRI contrast enhance agent, to the myocardium and used an MRI scanner to track the diffusion profile in real-time. A $4 \times 4\ cm^2$ block of myocardium was cut from a fresh explanted pig left ventricle all the way through the ventricular wall. A 15 ml truncated test tube was attached to the epicardium using adhesive (KEG-50 Starbond Flexible Thin CA Glue). 1 ml Dotarem (0.5 M) mixed with 9 ml of saline was placed in the test tube reservoir. The tissue block was immersed in saline. The whole setup, see Fig. 3-1(b), was put into a Siemens Skyra 3T scanner (Siemens Healthineers, Erlangen, Germany) for 14 hours, with scans every 15 minutes. Since the T1 relaxation rate is proportional to the Gadolinium (Gd) concentration, it can be used to calculate the relative Gd concentration in different regions, given that the concentration inside the reservoir is known (0.05 M). Thus, a T1 map was also acquired every 15 minutes at the mid cross-sectional plane in order to calculate the Gd concentration at the edge of the diffusion profile. The Diffusion Tensor Magnetic Resonance Imaging (DTI) technique was used to image the fiber orientation of the myocardial section.

We then used Mimics Research v.21 (Materialise NV, Leuven, Belgium) to reconstruct the myocardial tissue block and the Gd diffusion profile at each time frame. The fiber orientation map, which contained the primary eigenvector of each voxel after post-processing the DTI data, was superimposed with the tissue geometry and Gd profile, Fig. 3-2. The diffused distance was measured every hour along the fiber direction and sheetlet direction at the epicardium. The diffusion distance was also measured in the sheetlet normal direction, which is the transmural direction indicating how far the Gd penetrated through the myocardium, Fig. 3-3. In addition, we used the T1 map to find the concentration ratio between the diffusion edge and the reservoir to be 0.065. This made the edge concentration, also the minimum detectable concentration (MDC) to be 0.003 M. With these experimental measurements, the diffusion coefficient (D), also known as diffusivity, in each direction was calculated based

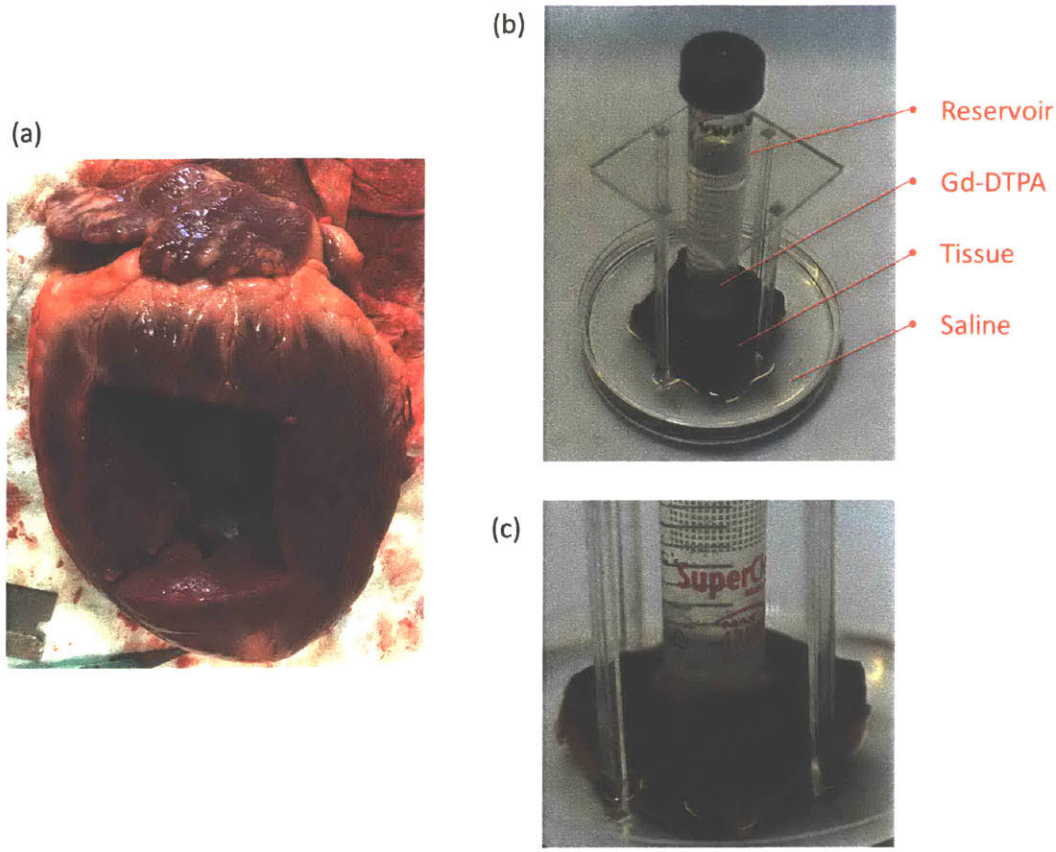

Figure 3-1: Gadolinium diffusion setup. (a) A 4×4 cm^2 tissue block through the wall was extract from the left ventricle. (b) A custom diffusion rig that was put into the 3T MRI scanner. (c) A closer view of the interface between the epicardium and the Gd reservoir.

on Fick's second law, see Equation 3.1. The diffusion coefficients calculated at every hour are plotted in Fig. 3-3(d), showing that the they vary significantly in the first 5 hours and eventually converge to a stage that the sheetlet diffusivity ((D_s)) and the sheetlet normal diffusivity (D_n) are similar and are about 58% of the value in the fiber diffusivity (D_f). In other words, the fiber-to-cross-fiber diffusivity ratio is 0.58. The diffusion coefficients at 14 hours were picked for the following simulations in this study, as 0.8979, 0.5641, 0.4161 mm^2/hr in the fiber, sheetlet normal and sheetlet directions, respectively.

$$n(x,t) = n_0 erf(\frac{x}{2\sqrt{Dt}}) \tag{3.1}$$

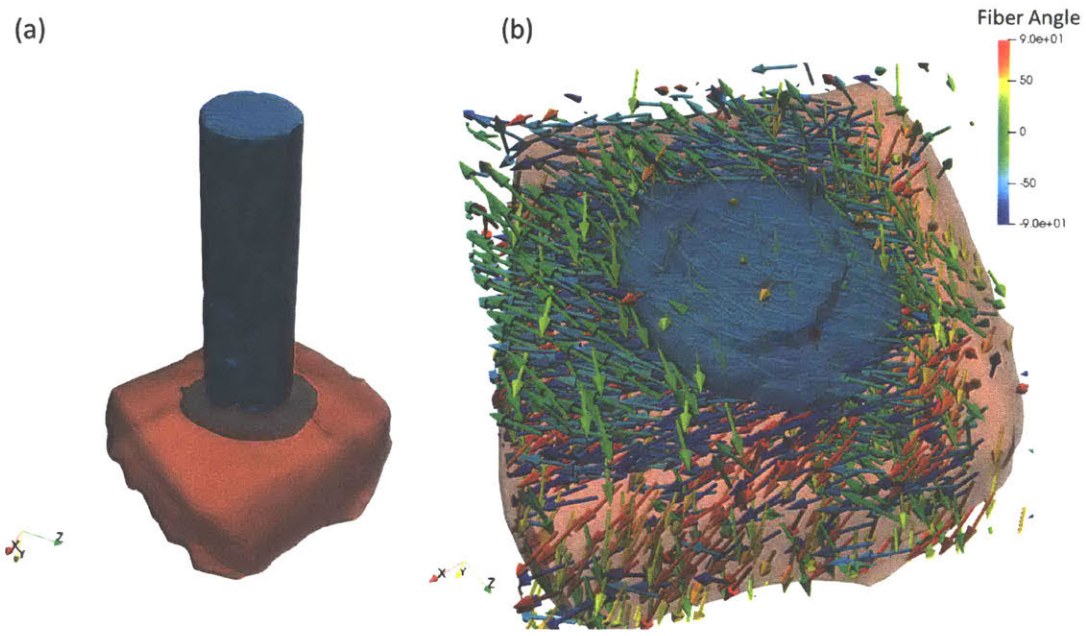

Figure 3-2: DTI reconstruction. (a) Reconstruction of the tissue geometry (red) and Gadolinium profile (blue) at 14 hour from MRI. (b) Superimpose of the geometries and the fiber structure. The latter is reconstructed from DTI data.

where n_0 is the initial (reservoir) concentration, n is the local transient concentration, t is diffusion time, x is diffusion distance, and erf is the complementary error function.

The diffusion finite element (FE) model was built using Abaqus 2018 (Dassault Systèmes, Vélizy-Villacoublay, France) [45]. The reconstructed geometry was imported from Mimics and discretized in Abaqus/CAE with 102339 tetrahedron elements (DC3D4). Next, following a previous study [46], the post-processed DTI data was mapped to the FE model by assigning the orientation of the closest data point to the integration points of each element as its local orientation using MATLAB (The MathWorks, Inc., Natick, MA, USA). Details of the FE model setup are shown in Fig. 3-4. A thermal analogy as previously described [31], with the governing Equation 3.2, was used to simulate the diffusion process. Table 3.1 shows the direct comparison

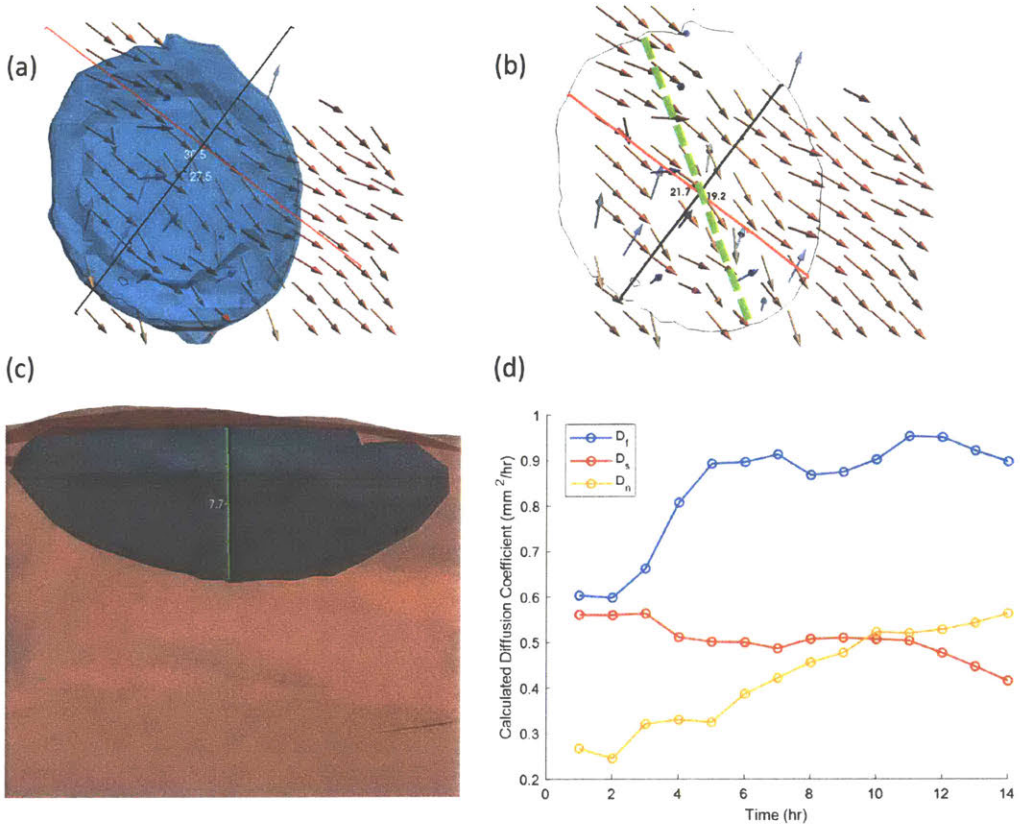

Figure 3-3: Diffusivity measurement. (a) The fiber direction (red) was aligned with the dominated fibers at the epicardium and rotated 90° to get the sheetlet direction (black). (b) The diffusion lengths in both directions were measured based on the diffusion profile. Green dashed line indicates the fastest diffuision direction. (c) The diffusion depth was measured as the diffusion length of the sheetlet normal direction (green). (a-c) show the diffusion profile at 14 hours. (d) The diffusion coefficients in the three directions were plotted against time.

between drug diffusion and thermal conduction. For most of the terms in thermal conduction, a direct analogy can be found in drug diffusion except for specific heat capacity. Here, we define it as the mass of drug to increase concentration in unit mass of tissue by one unit of concentration, and was set to 1 [31]. Using Equation 3.3, the diffusivities were converted to thermal conductivities ($mW/mm.K$), resulting in values of 2.49×10^{-13} (fiber), 1.16×10^{-13} (sheetlet), 1.57×10^{-13} (sheetlet normal). These values along with specific heat capacity and density ($1 \times 10^{-9}\ T/mm^3$) were assigned to the finite element (FE) model as the material properties of the myocardium.

The Gd concentration (0.05 M) was converted to a temperature (0.0377 K) using Equation 3.4 with a molecular weight of 753.861 g/mol for Dotarem. This was used as a boundary condition applied to the interface between the Gd reservoir and the epicardium. In this way, the reservoir is not explicitly modeled but rather we assumed that it is big enough that the concentration inside does not change significantly over the time we are modeling. The simulation was run using the Abaqus/Implicit solver. The predicted diffusion lengths were compared with the experimental diffusion profile measured from the MRI scans.

Table 3.1: Drug Diffusion vs Thermal Conduction

Drug Diffusion	Thermal Conduction
n: Drug concentration (t/t)	T: Temperature (K)
D: Drug diffusivity (mm^2/s)	α: Thermal diffusivity (mm^2/s)
ρ: Density (t/mm^3)	ρ: Density (t/mm^3)
C: Mass of drug to increase concentration in unit mass of tissue by one unit of concentration	c: Specific heat capacity $(mJ/t{\cdot}K)$
K: Drug diffusion coefficient $(t/mm.s)$	k: Thermal conductivity $(mW/mm{\cdot}K)$
M: Drug mass (t)	q: Heat (mJ)
$\dot{M}$: Drug generation rate per unit volume $(t/mm^3{\cdot}s)$	$\dot{Q}$: Heat flux $(mJ/s{\cdot}mm^3)$

$$\dot{Q} = -k\frac{dT(x)}{dx} \tag{3.2}$$

$$\alpha = \frac{k}{\rho c} \tag{3.3}$$

$$T = \frac{nM}{\rho} \tag{3.4}$$

where M is the molecular weight of the diffusing particles.

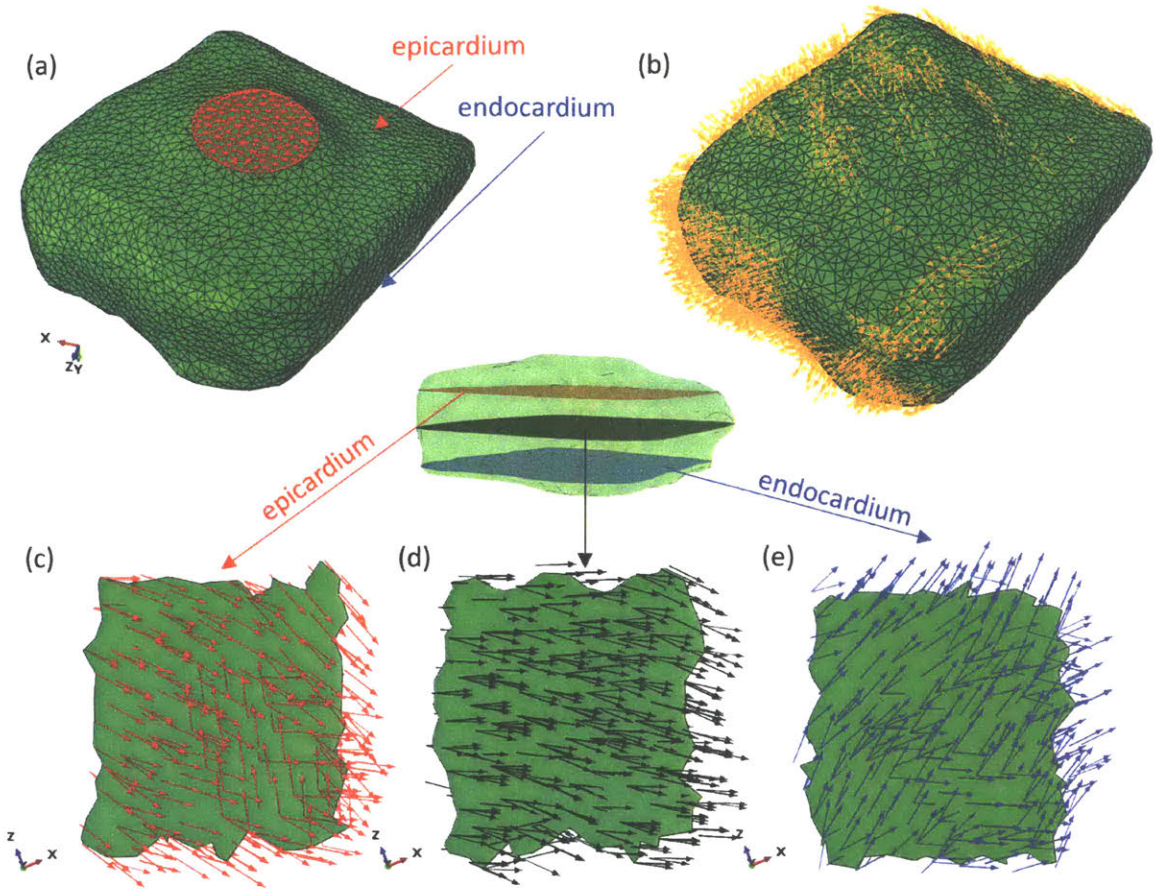

Figure 3-4: Finite element model of Gadolinium diffusion in myocardium tissue block. (a) 3D reconstruction and meshing of the myocardial tissue block. The surface marked in red indicates the interface between the Gd reservoir and tissue. (b) DTI data mapped on the FE model. (c-e) Fiber orientation at the epicardium (c), myocardium (d), and endocardium (e), which show the transmurally varying characteristics of myocardium structure.

Using a DTI dataset of a healthy pig left ventricle, a subject-specific FE model of the LV was developed following the same work-flow as the tissue block study, see Fig. 3-5. The calibrated diffusion coefficients were used in this study except that the sheetlet and sheetlet normal diffusivity were set to equal values as the myocardium is generally assumed to be transversely isotropic [47, 48, 49, 46]. One or multiple reservoirs were attached to the free wall of the left ventricle and the diffusion process were simulated up to 10 days, Fig. 3-6. Next we conducted a parameter study using this single reservoir. We looked at the effects of changing size and changing orientation on diffusion profile were explored. This study included models of three different sizes

of circular reservoir interface (radius of 5, 10, and 15 mm) and a further study included elliptical interfaces (15 and 7.5 mm in the long and short axes respectively) with the long axis aligned, perpendicular, or neutral to the epicardial fiber orientation. For multiple reservoirs, patterns of three to five circular reservoirs (radius of 7.5 mm) were simulated to predict their effect on diffusion profiles over time.

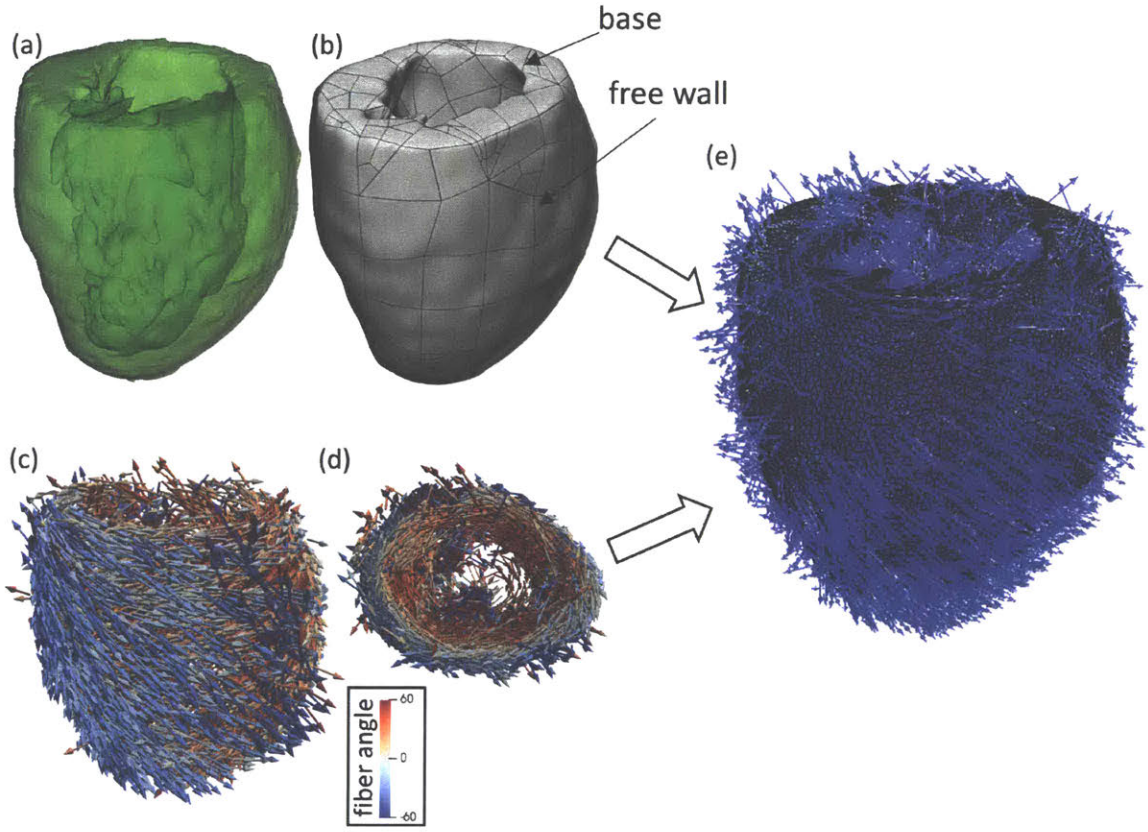

Figure 3-5: The process of developing a subject-specific left ventricle finite element model. The MRI data was (a) segmented in Mimics to identify the LV geometry and (b) discretized in 3-Matic. The geometry was imported to Abaqus for meshing. (e) Finally, MATLAB was used to map the DTI data (c - LV free wall, d - LV base) to the FE mesh.

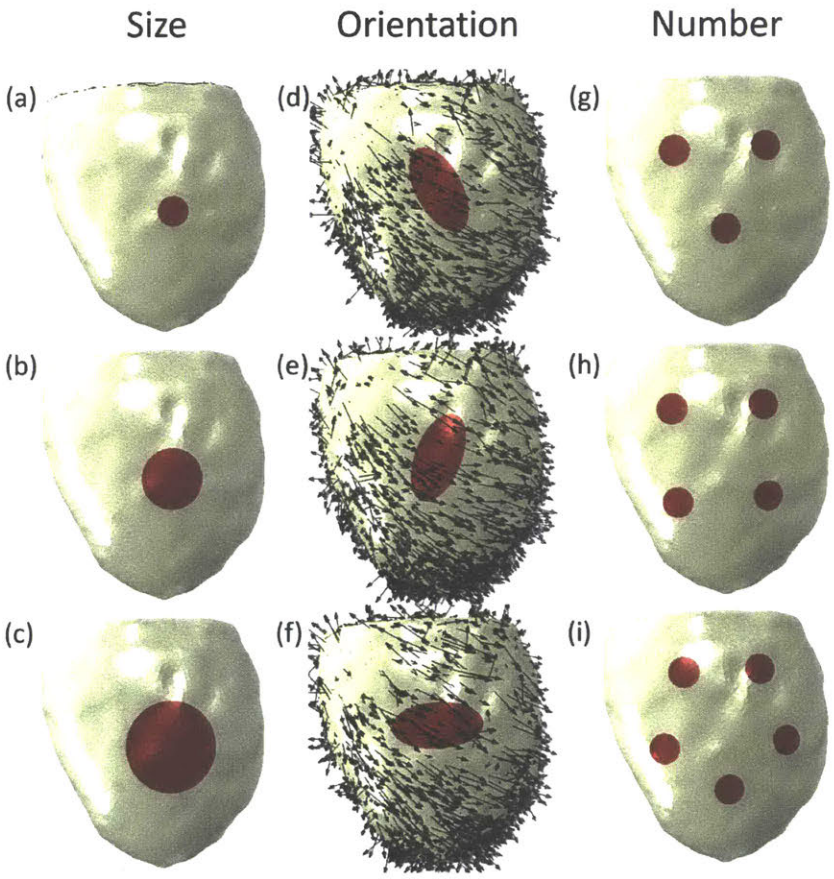

Figure 3-6: An overview of the different design of the drug reservoir for epicardial delivery. Single reservoir designs, where the size was changed (a-c), or the orientation was changed (d-f). The long axis of the ellipse reservoir was either aligned (d), perpendicular (e), or neutral (f) to the epicardial fiber orientation. The patterns and spatial positioning of multiple reservoirs(g-i).

3.2 Results

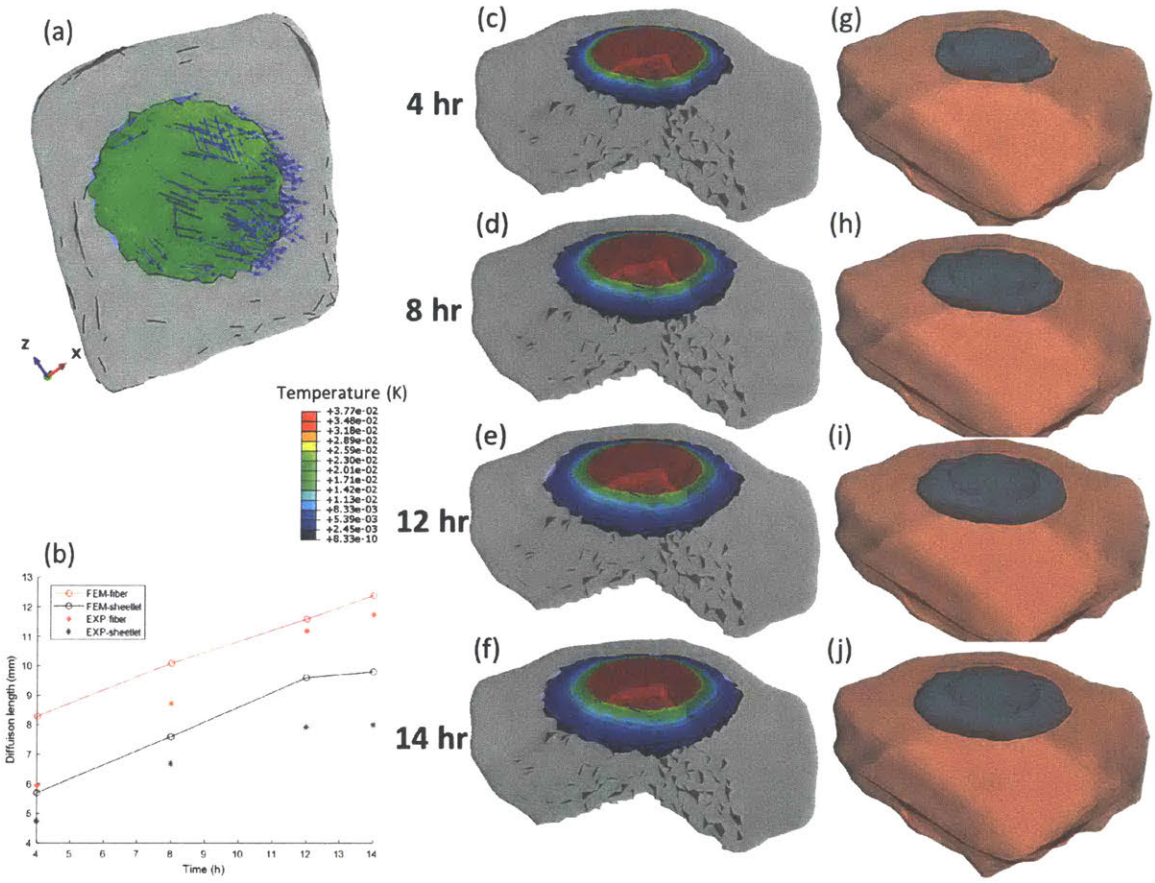

Figure 3-7: A comparison of the Gd diffusion profile between FE prediction and MRI measurement. (a) The predicted diffusion profile after 14 hours superimposed with fiber orientation. (b) A comparison of the diffusion lengths between FE predictions and MRI measurements. Counter plots of the predicted Gd concentration at different time points (c -f) and their corresponding MRI profiles (g-j).

The FE prediction of Gd diffusion profiles are shown in Fig. 3-7 compared to the experimental measured profiles reconstructed from MRI. The predicted profiles are shown by truncating elements with temperature lower than 0.00245 K, which corresponds to the minimum detectable Gd concentration (0.003 M) that was calculated from the T1 map. After 14 hours of diffusion, the predicted profile at the epicardium was an ellipse with the long axis following the epicardial fiber resulting from the anisotropic diffusivities ($D_s : D_f = 0.58$). The predicted diffusion lengths in the fiber and sheetlet directions were calculated and compared to the corresponding

experimental measurements. According to Fig. 3-7(b), the FE model consistently over predicted the diffusion lengths in both directions. This can also be seen in the 3D profiles in Fig. 3-7(c-j).

Looking at the results of the study where the size of the reservoir was varied, all cases showed the anisotropic profile at the epicardium, Fig. 3-8. For all three cases, the long axis of the elliptical profile followed the fiber orientation at day 1 but gradually became more circumferential as diffusion progressed further. Comparing with different sizes, the bigger the reservoir interface is, the further it can diffuse in the same time. This is true not only in the fiber and sheetlet direction, but also in the sheetlet normal direction, where the transmural penetration is much faster with the 15 mm reservoir than the 5 mm, see Fig. 3-9.

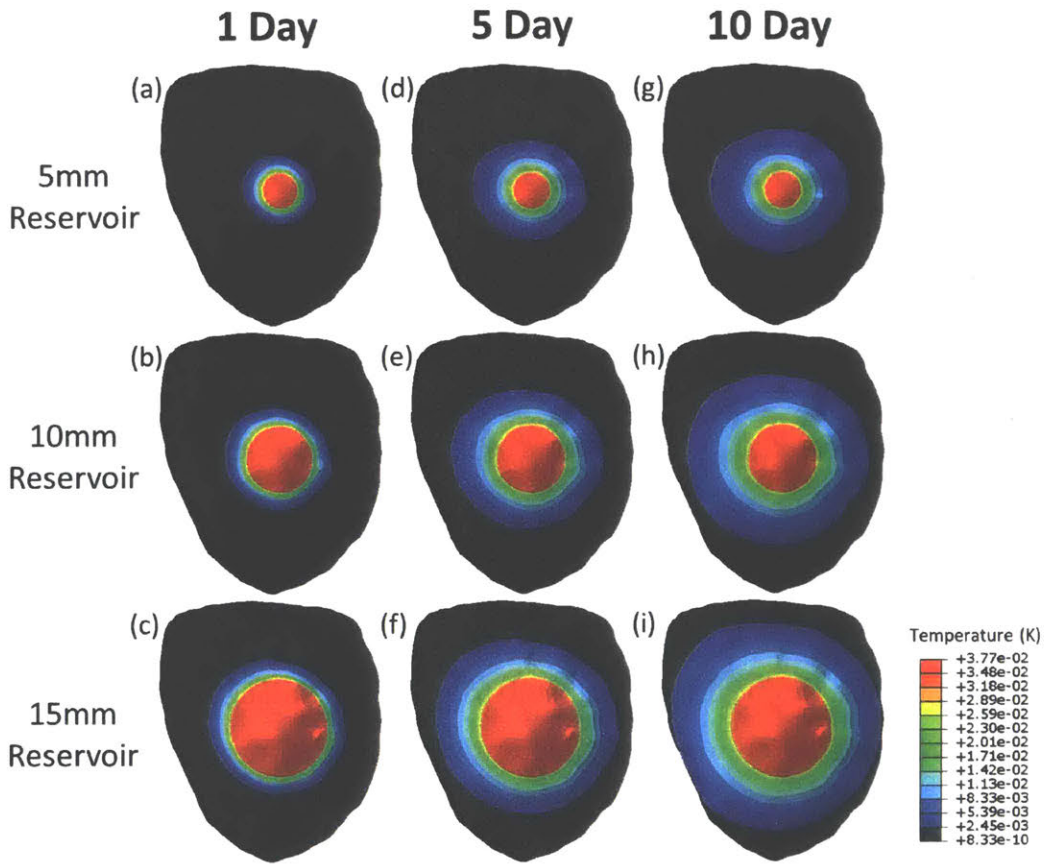

Figure 3-8: Concentration counter plots of the predicted diffusion profiles at the epicardium. The profiles after 1 day (a - c), 5 days (d -f), and 10 days (g - i) of diffusion are shown for each of the three reservoir designs.

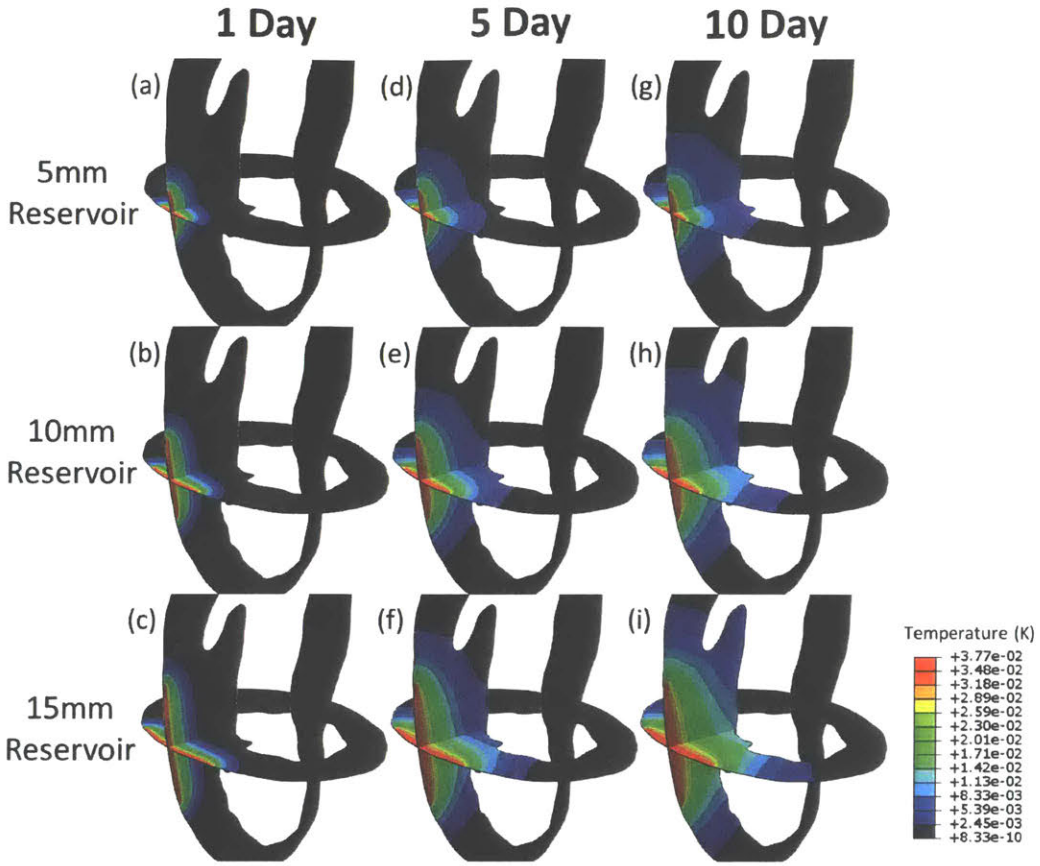

Figure 3-9: Concentration counter plots of the predicted diffusion profiles at the LV long axis and short axis planes. The profiles after 1 day (a - c), 5 days (d -f), and 10 days (g - i) of diffusion are shown for each of the three reservoir designs.

According to the results of the spatially varying models, see Fig. 3-10, the epicardial diffusion profiles followed the shape of the reservoir after 1 day. After 5 days of diffusion, the anisotropy of the profile increases in the fiber orientation while decreasing in the perpendicular orientation. In the case with neutral orientation, the profile still followed the elliptical shape but started to elongate along the fiber direction. The transmural penetration was not significantly different between these three cases.

The results of the multiple reservoir study are shown in Fig. 3-11. Since the distance between reservoirs was closer in the 5-reservoirs case than the other two cases, the diffusion profiles merged between each other in the former case after 1 day while the other two did not. After 5 days, the diffusion profiles of the 4 and 5-reservoir cases covered almost the entire LV free wall. For all three cases, the diffusion could

penetrate the wall after 5 days.

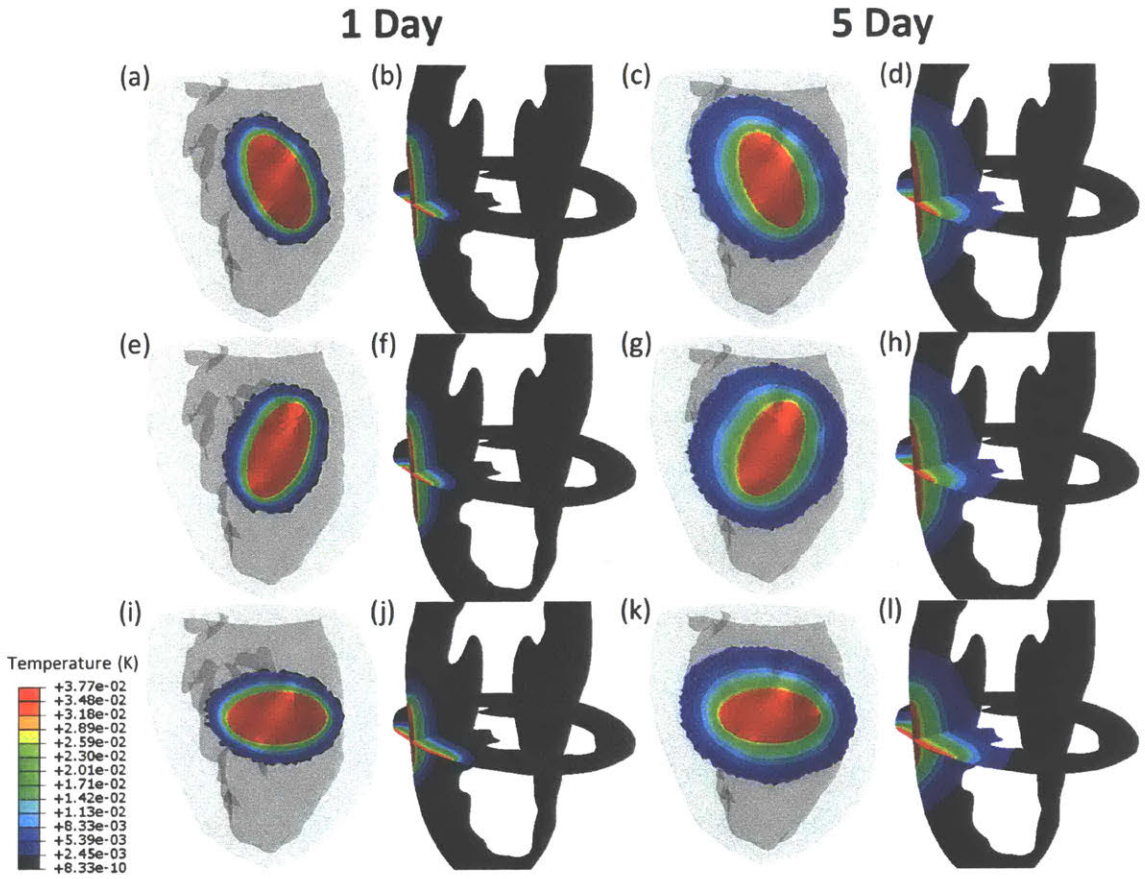

Figure 3-10: Diffusion profile predictions in the orientation study. Concentration contour plots of the reservoirs that are aligned (a-d), across (e-h), or neutral to the epicardial fiber orientation.

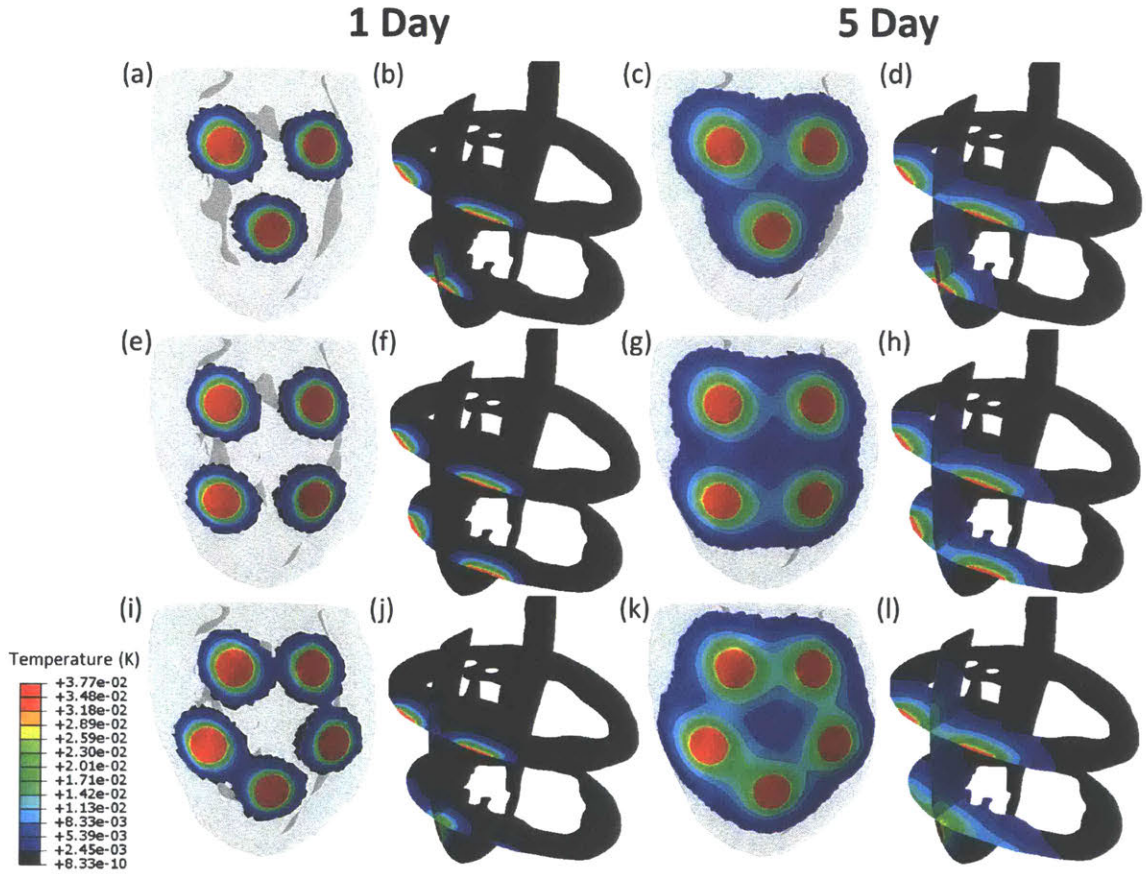

Figure 3-11: Diffusion profile predictions in the multiple reservoir study. Concentration contour plots of the designs with 3 (a-d), 4 (e-h), or 5 (i-l) reservoirs.

3.3 Discussion

Although the DTI technique is based on the theory that the diffusion of water molecule is anisotropic in the myocardium, to our knowledge, there is no reported work using it to study the drug diffusion pattern in myocardium. Gleason et al. [50] used MRI to track the diffusion of Gadolinium, a MRI contrast agent, from the pericardium to the myocardium. More recently, MnO-based nanoparticles, injected systemically, were tested as an alternative MRI contest agent and potential drug vehicle [51]. These studies show that cardiac MRI could be an important technique to study the drug transport mechanism in the myocardium and also to improve the precision and efficiency of local myocardial drug delivery.

In this study, we successfully used MRI to track the dynamic diffusion of Gadolinium in myocardial tissue and used DTI to illustrate the fiber structure of the same tissue. The Gd profile from MRI confirmed our hypothesis that diffusion in myocardium is anisotropic and is faster along the fiber direction. The diffusion coefficients calculated by Fick's law showed that the diffusivity was increasing in both the fiber and sheetlet normal directions while decreasing in the sheetlet direction overtime, especially in the first 5 hours. The variation could come from (i) the errors introduced by manual measurements of diffusion lengths or (ii) from the segmentation of the Gd profile. The segmentation was done by picking a pixel intensity range to threshold the interested object. This can be difficult especially at the beginning of the study because very little Gd had diffused into the tissue and the edge between Gd and non-Gd tissue is hard to find due to high signal-to-noise ratio. Therefore, the diffusivity calculated at a longer time point should be more accurate and the convergence shown in Fig. 3-3(d) confirms this. Also, the sheetlet diffusivity decreased over time could result from dehydration of the tissue after sitting inside the scanner for 14 hours. The diffusivity was higher in the sheetlet normal direction than in the sheetlet direction. This could result from the natural myocardium anisotropy since a recent DTI study [24] has shown that the myocardium is entirely anisotropic rather than transversely isotropic, which has been assumed in many previous cardiac simulations [47, 48, 49].

The force applied by the large among of Dotarem solution on top of the tissue also increased Gd transportation rate in the vertical (sheetlet normal) direction. This gravity effect could also contribute to the difference of diffusivity in the two cross-fiber directions. Therefore, in the LV simulations, the lower diffusivity (sheetlet) was chosen as the cross-fiber diffusivity not only to increase the anisotropic effect but also assuming that gravity factor has less effect on the sheetlet diffusivity. Another factor that can change the magnitude of the diffusivity is the minimum detectable concentration (MDC).

In the tissue block simulation, we have successfully converted the MRI-based 3D geometry into an FE model and combined it with fiber orientation from the DTI data. The model is able to show anisotropic diffusion as we hypothesized and confirmed with the MRI images. The over predictions of the FE model may stem from the error of the diffusivity which is discussed above. Moreover, the MDC is another determinant of the FE predictions. In this study, MDC was found to be 3 mM. However, the MDC of Dotarem in a 7 Tesla MRI machine was found to be 3.1×10^{-3} mM [52], which is 3 orders of magnitude smaller than our MDC. If this much smaller MDC was used, the diffusivities will slightly reduce but the minimum cut off in the concentration contour plot will be reduced significantly, leading to further over prediction. In order words, by increasing or reducing the MDC, the FE model can over or under predict the diffusion profile, respectively. In addition, the mapping between the FE model and DTI data could change the fiber structure in the simulation depending on the DTI resolution as well as the FE mesh quality. This can also significantly affect the diffusion profile prediction. Finally, and most importantly, the fastest diffusion axis did not exactly align with the fiber direction as shown in Fig. 3-3(b). Therefore, applying the fastest diffusivity along the fiber direction in the model will lead to over prediction. Interestingly, the misalignment was also shown in the LV diffusion models, 3-8. The transmurally varying structure of the fiber orientation might be the reason for this misalignment but further investigations are needed to confirm this hypothesis.

The discussion above elaborated that the diffusivity and the diffusivity ratio be-

tween the fiber and cross-fiber direction highly depend on the image segmentation, diffusion length measurement, and calculation of minimum detectable concentration. Each of these factors has potential to introduce errors to the final diffusivity values. Therefore, we also conducted a sensitivity study of diffusivity on a simple cubic model with transmurally varying local element orientation to guide how to adjust the diffusion coefficient to match the experimentally measured drug diffusion profile, see Appendix A.

Another interesting correlation we found in this study is the similarity between the fiber-to-cross-fiber diffusivity ratio (DR) and the eigenvalue ratio (ER) from the DTI data. For the tissue block, the DR is 0.58 and the ER is 0.54. The ER from the pig LV DTI data, used in this study, is 0.61. Another rat heart DTI dataset, provided by Irvin et al. [23], also shows a similar ER value of 0.57. Therefore, we believe that there is a strong correlation between the diffusivity ratio and eigenvalue ratio. The implications of this could be that future studies can calculate the diffusivity in the fiber direction and use the ER from DTI data to interpret the diffusivity in the cross-fiber directions.

According to the LV diffusion studies, which showed the diffusion profiles of various reservoir designs, we found that the transmural penetration speed depended largely on the area of the reservoir interface. Changing the orientation of the reservoir or adding multiple reservoir did not have a significant effect. The shape and orientation of the reservoir can be adjusted to change the diffusion length in the circumferential and longitudinal directions to achieve desired diffusion profiles. The multiple reservoir design can be used to increase the effective region of drug within the same amount of time.

Although these LV models have successfully showed the anisotropic diffusion process in myocardium, there are a few limitations in the models. First of all, constant concentration was assumed in the reservoir which might not be representative especially for modeling the Therepi device where the reservoir is relative small benefiting from its refill-able design feature. This issue can be addressed by applying time dependent temperature boundary condition to the reservoir interface. The temperature

changes can be calculated using Equation 3.2 with nodal heat flux values at the interface. Temperature can be updated in each time increment by menas of the URDFIL user subroutine in Abaqus. Another limitation comes from the fact that the model did not consider the other drug transportation mechanisms (advection and binding) that happens in the myocardium simultaneously with diffusion. According to the LV simulations, the diffusion is slow, taking a number of days for the Gd to penetrate through the ventricular wall. Convection, due to the blood flow in coronary arteries and myocardial capillaries, is a relatively faster mechanism that might dominate the drug transportation. It might also quickly drain the drug in the epicardium, which has been shown in an *in vivo* study [3]. Binding with proteins is another mechanism that happens with drugs but not with contrast agent, and therefore was not considered in our model. Both convection and binding are the mechanism that have negative impact on the drug concentration in myocardium. Therefore, a simplified approach to account for these factors could be to give a negative heat flux (Q) in the myocardium to replicate a "global heat sink".

In conclusion, this is a work-flow that can be used to characterized the anisotropic diffusion of different drugs in the myocardium. We also validated this which is significant as many of the previous drug transport modelslack validations [31, 32, 35, 34]. The DT-MRI technique could be a good technique to validate the diffusion model. For simulating the drug transportation in the heart, other mechanisms such as blood flow convection and drug binding with proteins need to be considered in the model. Therefore, more *in vivo* studies delivering actual drugs might be required to characterize the properties of these drug transport process.

Chapter 4

Characterization of "fibRobot"

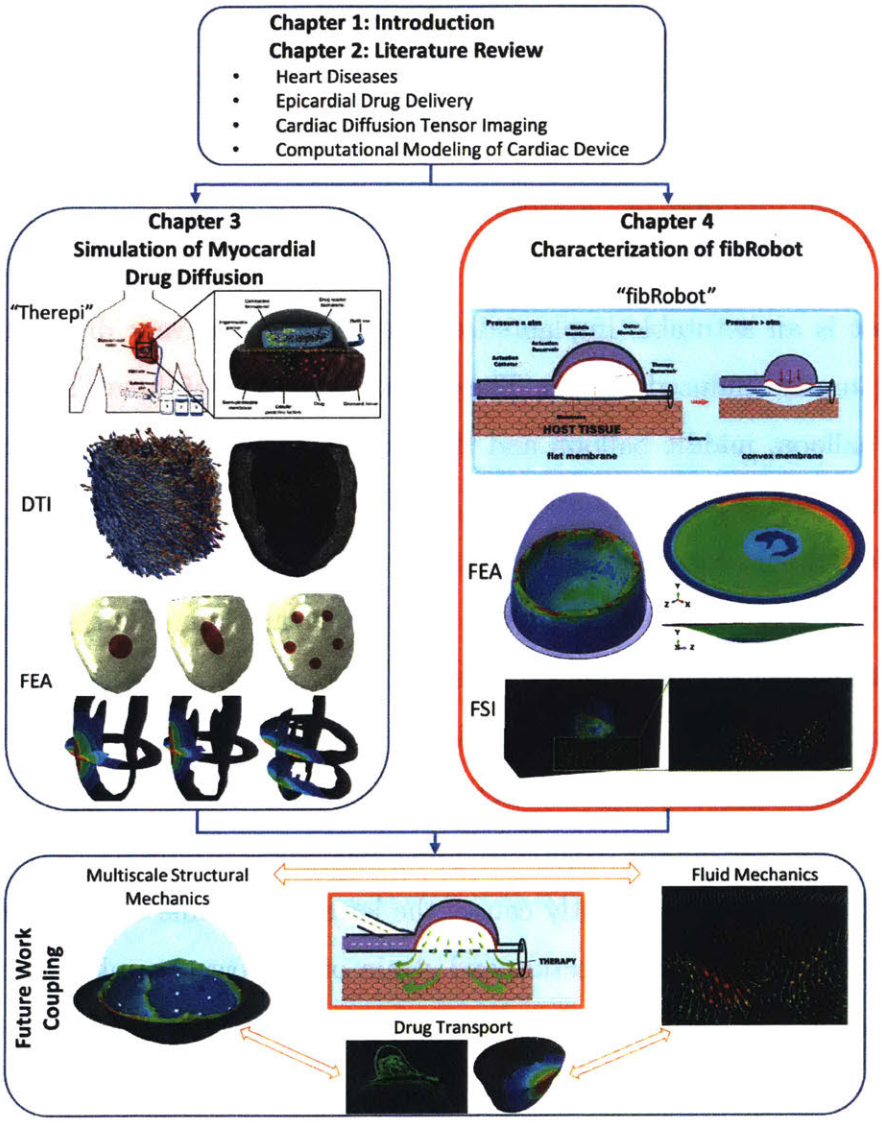

4.1 Method

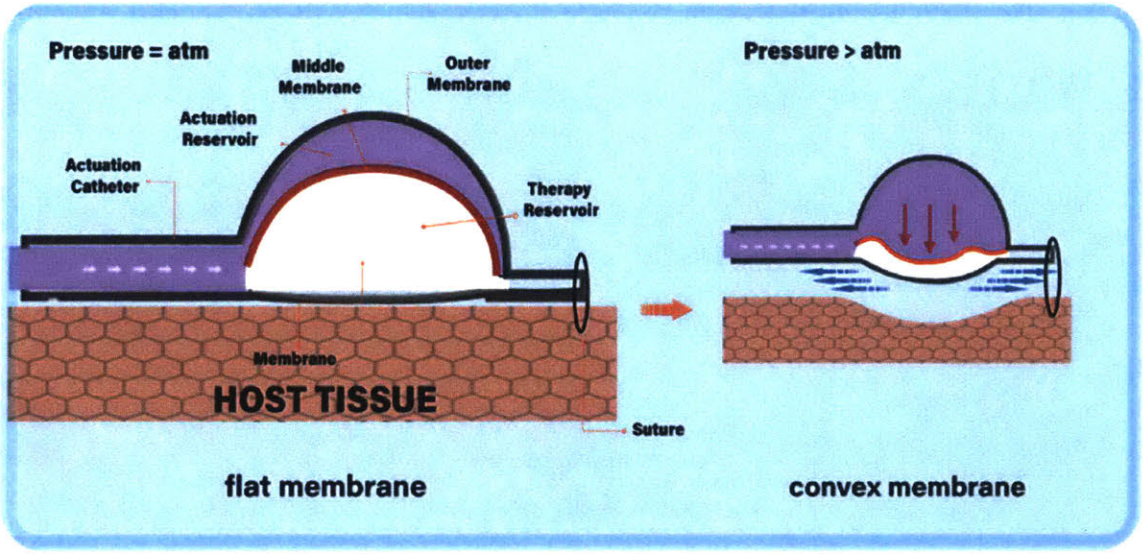

Figure 4-1: An overview of "fibRobot". The design of the device (left) and the actuation mechanism (right).

fibRobot is an actutable implanted device that can delivery drug locally while alleviating implant-induced fibrosis. The device is made out of three TPU membranes, the outer balloon, middle balloon and the lower membrane, each with thickness of 12 mil, 3 mil and 3 mil, respectively. (1 mil is defined as 0.001 inch.) The outer and middle balloons form the actuation chamber that is connected to an actuation catheter. The middle balloon and lower membrane can form either a drug reservoir or a closed chamber depending on whether the lower membrane is porous or not. The proposed mechanism of action of the device is shown in Fig. 4-1. When the actuation reservoir is pressurized through the actuation catheter, the volume, of the chamber increases, causing the middle balloon to invert and deflect downward (red arrows), see Fig. 4-1(right). This subsequently causes the lower membrane to deflect downward. Actuation therefore causes deflection and strain of the lower membrane, and results in fluid flows at the tissue interface which affects cell adhesion and initiation of the fibrotic response. By implanting the device subcutaneously a rat model, we have experimentally shown that the device attenuated the progression of foreign body

response [7]. Here, in order to elucidate the anti-fibrosis mechanism, we used finite element simulation to evaluate the stress and strain provided by the device and used fluid structure interaction technique to demonstrate the fluid flows surrounding the lower membrane.

All simulations were conducted using Abaqus 2018 (Dassault Systèmes, Vélizy-Villacoublay, France) [45]. Since the fibRobot is made out of thin TPU sheets, shell structural analysis was chosen for the simulation. The device was modeled as a 3D surface geometry, which contains the outer balloon, the middle balloon and the lower membrane, as shown in Fig. 4-2. The outer and middle balloons were half ellipsoids with the same short axis (2.25 mm) and slightly different long axes, 4.5 mm and 4.4 mm, respectively. The lower membrane was a circular flat shell with radius of 2.5 mm. The corresponding thickness of each shell, as mentioned above, was assigned along with a material model for each. All parts were meshed with 6625 four-node shell elements (S4R). The dirichlet boundary condition was applied to the protruding edge of the lower membrane and the rest of the structure were allowed to deform freely. A 2 psi ramp loading was applied to the internal surface of the outer and middle balloons for a duration of 500 ms. These boundary conditions were applied in order to represent the setup of the device in the animal experiment where the device was sutured on the tissue through the lower membrane edge and was actuated with a cyclic pressure with magnitude of 2 psi and a frequency of 1 Hz.

In order to find a suitable material model for the TPU sheet, ASTM D638 uniaxial tensile tests were performed with laser cut TPU specimens, both porous and non-porous, on a ZwickRoell material testing machine. Using the material evaluation function in Abaqus, four hyperelastic constitutive models (Neo-Hookean, Mooney-Rivlin and Ogden 3rd order, Yeoh) were evaluated. The strain energy density function of each model are shown in Equations 4.1 - 4.4, respectively. As shown in Fig. 4-3(c), the Ogden 3rd order model has the best curve fitting performance and therefore was used. The curve-fitted parameters are shown in Table 4.1

Neo-Hookean:

$$U = C_{10}(\bar{I}_1 - 3) \tag{4.1}$$

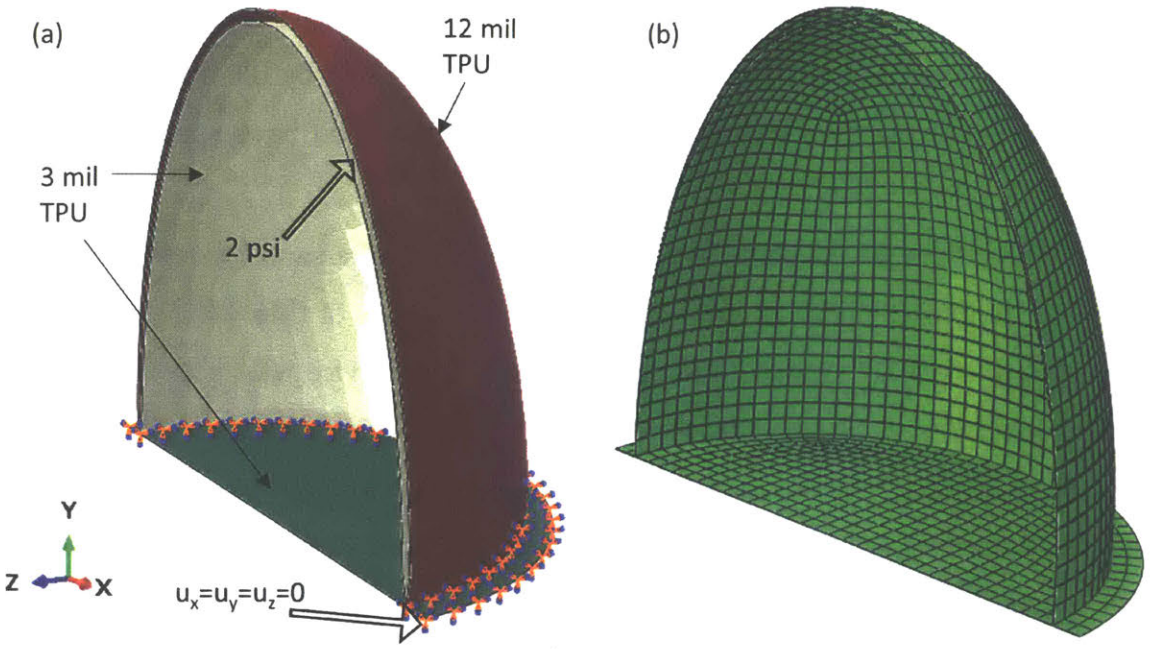

Figure 4-2: Finite element model overview. (a) CAD drawing of the fibRobot with indicated boundary conditions on outer balloon (red), middle balloon (white) and lower membrane (green). (b) The FE mesh of fibRobot.

Mooney-Rivlin:

$$U = C_{10}(\bar{I}_1 - 3) + C_{01}(\bar{I}_2 - 3) \tag{4.2}$$

where C_{10} and C_{01} are material parameters; $\bar{I}_1$ and $\bar{I}_2$ are the first and second deviatoric strain invariants defined as:

$$\bar{I}_1 = J^{-\frac{2}{3}} I_1 = J^{-\frac{2}{3}} \lambda_1^2 + \lambda_2^2 + \lambda_3^2$$
$$\bar{I}_2 = J^{-\frac{4}{3}} I_2 = J^{-\frac{2}{3}} \lambda_1^2 \lambda_2^2 + \lambda_2^2 \lambda_3^2 + \lambda_3^2 \lambda_1^2$$

Ogden:

$$U = \sum_{i=1}^{N} \frac{2\mu_i}{\alpha_i^2} (\bar{\lambda}_1^{\alpha_i} + \bar{\lambda}_2^{\alpha_i} + \bar{\lambda}_3^{\alpha_i} - 3) \tag{4.3}$$

where $\bar{\lambda}_i$ are the deviatoric principal stretches $\bar{\lambda}_i = J^{-\frac{1}{3}} \lambda_i$; N, μ_i, and α_i are materials parameters; μ_i is related to shear modulus as $u = \sum_{i=1}^{N} \mu_i$.

Yeoh:

$$U = C_{10}(\bar{I}_1 - 3) + C_{20}(\bar{I}_1 - 3)^2 + C_{30}(\bar{I}_1 - 3)^3 \tag{4.4}$$

where C_{10}, C_{20}, and C_{30} and material parameters.

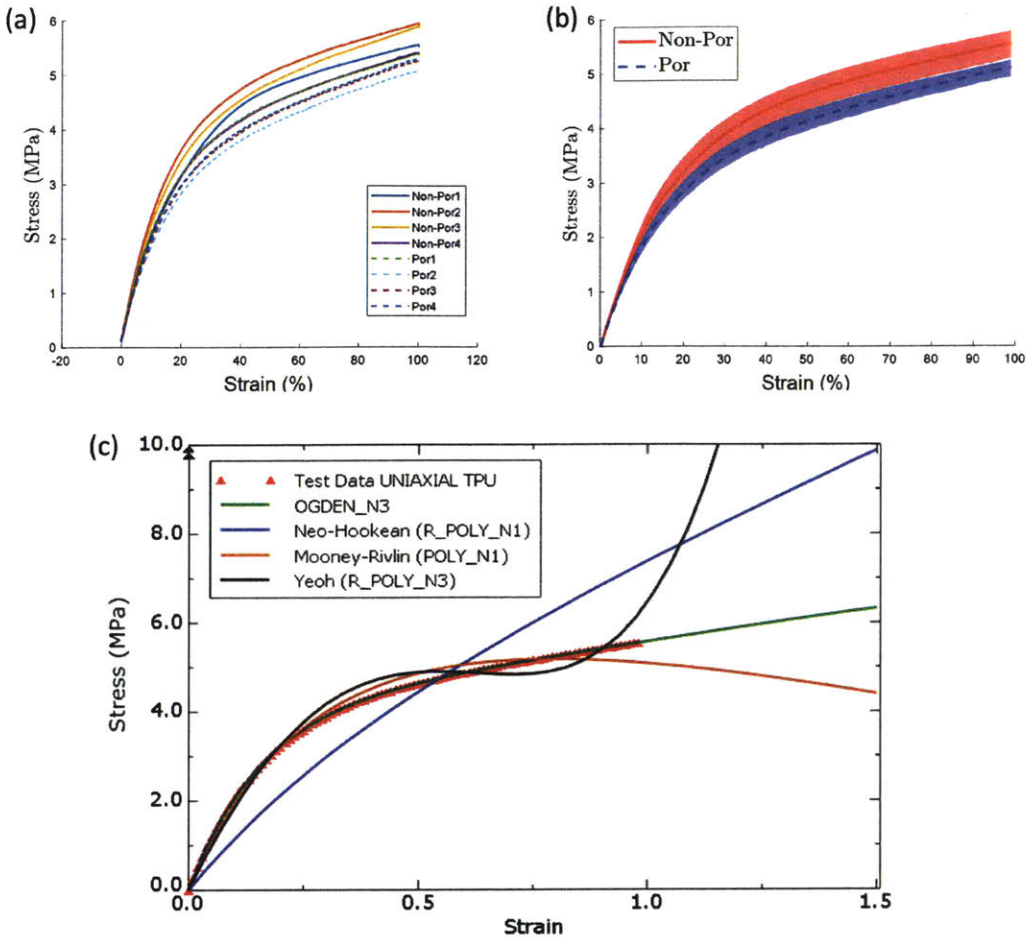

Figure 4-3: Evaluation of constitutive models for TPU. (a) Stress vs. strain curves of porous and non-porous 3mil TPU samples. (b) Averaged stress vs. strain curves. (c) Curve fitting of different hyperelastic model to the averaged non-porous stress curve.

Table 4.1: Curve-fitted parameters of Ogden 3rd order model

i	μ_i	α_i
1	-8.31	0.46
2	-0.36	3.62
3	17.89	-3.10

In order to validate the FE model, the actuation force of the device was measured using the Instron 5944 material testing machine (Instron, MA, USA). The setting is shown in Fig. 4-4. The actuation catheter was connected to a custom built pneumatic

control box which can generate cyclic pressure to actuate the reservoir. As shown in Fig. 4-4(c), the device was rotated 180° with the membrane edge adhered on top of an acrylic holder. The thickness of the acrylic piece and the diameter of the hollow cylinder were larger than the height and the diameter of the outer balloon which allowed it to deform freely. The distance between the two Instron heads were fixed a height slightly greater than the height of the acrylic piece to allow insertion. A range of pressures (1 - 8 psi) were applied by the control box to actuate the device in 1 Hz. The actuation force was measured using a 50 N load cell. For the purpose of recreating the same setup as in the *in vivo* study, we were mostly interested in the pressure around 2 psi which is close to the lower limit of the control box capability. Therefore, the pressure was also monitored with a pressure sensor (ArgoTrans Model 2 / Neonatal, Argon Medical Device Inc., TX, USA) at the connection, see Fig. 4-4, in case there was any pressure fluctuation from the control box regulator or pressure loss along the pipeline connections. LabVIEW 2017 (National Instruments Corporation, TX, USA) was used both to manipulate the control box and to record data from the pressure sensor.

Based on the FE model, we also created an FSI model using the smooth particle hydrodynamics (SPH) technique to study the effect of surrounding flow during actuation, see Fig. 4-5. A region of dimensions $20 \times 20 \times 5mm^3$ was created and filled with 8000 particles. The particles were assigned with the following properties, density of 9.96E-7 kg/mm3, bulk modulus of 2.094 GPa and dynamic viscosity of 3.56e-8 MPa.s to represent interstitial fluid. Contact pairs were initiated between the shell structure and the particles. Loading and boundary conditions of the shell were the same as the structural analysis.

Since the main area of interest is the strain field of the lower membrane, the FE model can be simplified as a clamped circular membrane with distributed pressure in the transverse direction. In fact, this is a well known case in the field of shell theory that has been studied over the past century with various analytical approximations proposed [53]. In this study, we used the analytical approximation of a large deflection plate proposed by Zhang [53] to do a parametric study. All design parameters were

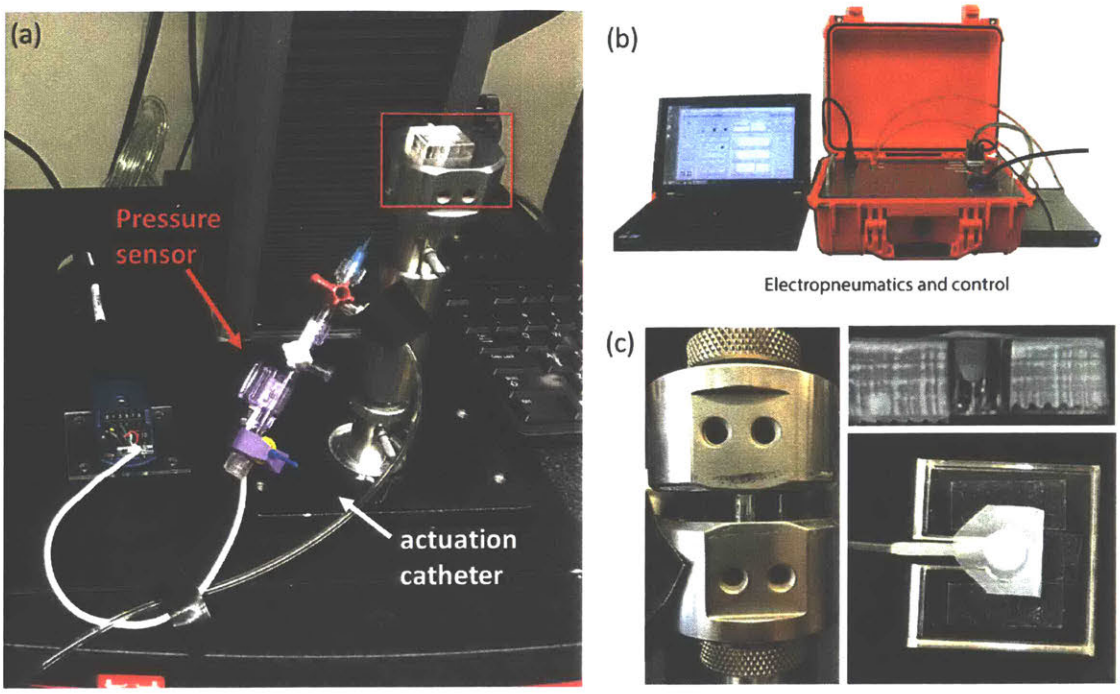

Figure 4-4: Setup for measuring actuation force. (a) An overview of the full setup. (b) Custom control box that is connected to the actuation catheter. (c) The acrylic holder for supporting the reservoir and ensuring that the lower functional membrane was in contact with the upper cross-head.

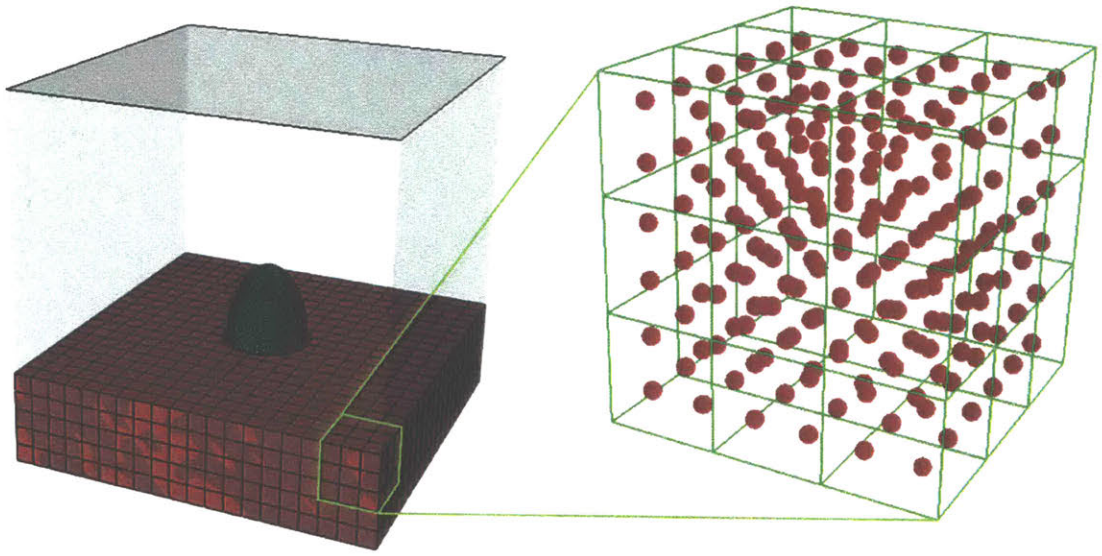

Figure 4-5: FSI model with smooth particle hydrodynamics (SPH). Each solid element is converted to 8 mesh free particles (left).

set according to the lower membrane of the fibRobot expect for the material model, which was assumed to be linear elastic with a Young's modulus of 15 MPa and a Poisson's ratio of 0.35. The effect of loading pressure (q), size (a), thickness (h), and material stiffness (E) of the membrane on the strain were evaluated. The details of this analytical approximation is illustrated in the following text; based on the von Kármán plate theory [54], the strain-displacement relations of a edge-clamped circular plate are given as follows:

$$\epsilon_r = \frac{N_r - vN_t}{Eh} = \frac{du}{dr} + \frac{1}{2}(\frac{dw}{dr})^2 + \epsilon_o \tag{4.5}$$

$$\epsilon_t = \frac{N_t - vN_r}{Eh} = \frac{du}{dr} + \epsilon_o \tag{4.6}$$

where u, w are the displacement in the radial and tangential directions respectively, a and h are the radius and thickness of the plate, and ϵ_o is the pre-stretch strain.

As a clamped plate, the deflection is assumed to follow Equation 4.7 which satisfies the boundary conditions of a clamped plate, $w(0) = 0$ and $\frac{dw(0)}{dr} = 0$. The maximum deflection (w_0) and radial displacement (u) become Equation 4.8 and 4.9 derived with the principle of virtual work.

$$w = w_o(1 - \frac{r^2}{a^2}) \tag{4.7}$$

$$\frac{3}{4}(\frac{a}{h}^2)(1+v)\epsilon_o w_0 + \frac{1}{2}(1+v)\frac{w_o^3}{h^2} = \frac{qa^4}{64D} \tag{4.8}$$

$$u = \frac{(5-3v)w_o^2}{6a^2}r + (v-3)\frac{w_o^2}{a^4}r^3 + \frac{(10-2v)w_o^2}{3a^6}r^5 + \frac{(-7+v)w_o^2}{6a^8}r^7 \tag{4.9}$$

4.2 Results

The real-time pressure monitoring shows that the control box initially overshoots the input pressure by up to 100%. The higher the input pressure is, the smaller the overshoot is. With the two low pressure regimes (1 and 2 psi) that were used in *in vivo* studies, the initial overshoot is about 98.9% and 56.0%, respectively. The actuation force measurements, up to an input pressure of 6 psi, shows an excellent match to the computational results, as shown in Fig. 4-6(b). Thus, these results validate the FE model. The real-time force measurements of different pressure regimes and their corresponding FEA predictions are shown in Fig. 4-6(c,d).

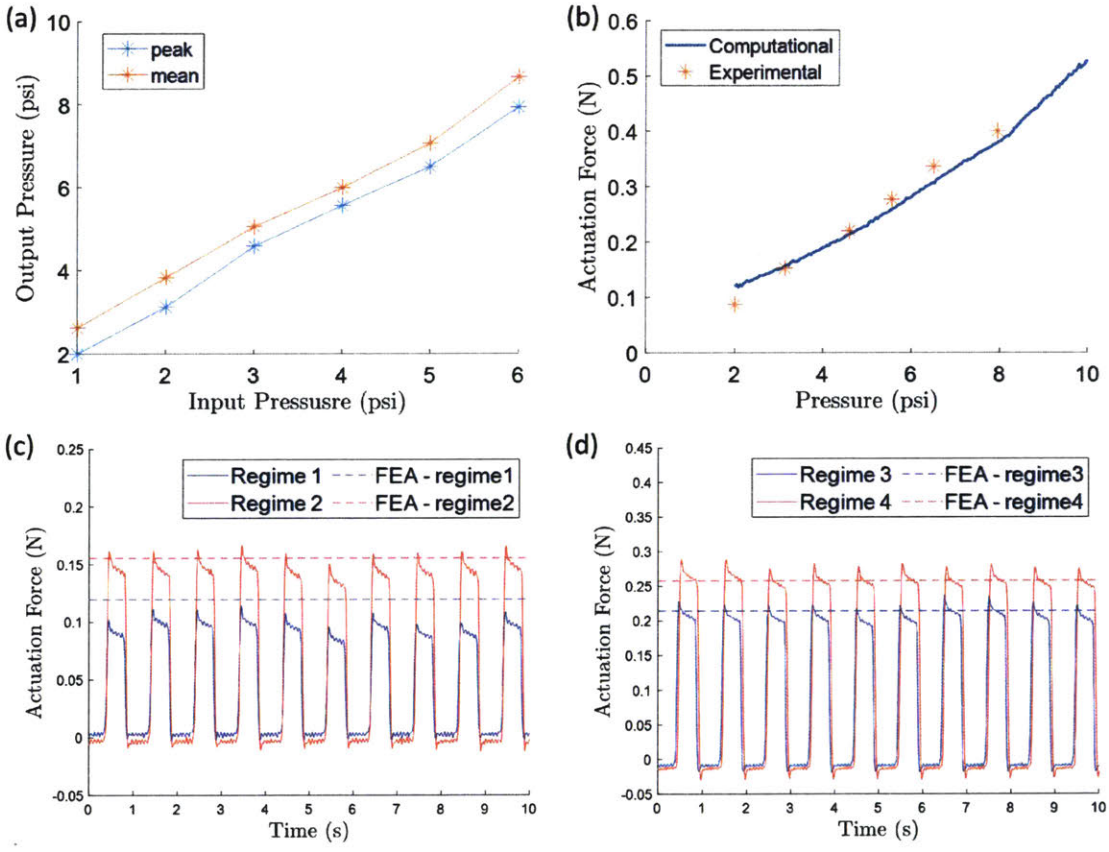

Figure 4-6: FE model validation. (a) A plot of receiving pressure vs. input pressure. (b) FE predicted actuation force compared with experimental measurements. (c) and (d) are the real-time cyclic actuation force measurements at the low and high regimes of input pressure, respectively.

From the FEA results, Fig. 4-7, stress and strain are much higher in the inner

balloon than the lower membrane. The stress concentration is around the buckling regions in which the maximum in-plane strain can go up to 38%. For the lower membrane, the strain (up to 7%) and stress (up to 2 MPa) are lower. The maximum vertical deflection is predicted to be 0.38 mm. Comparing the results between non-porous and porous membranes in Fig. 4-8, the later has slightly higher stress and strain as it is less stiff showing from the tensile testing data, Fig. 4-3(b).

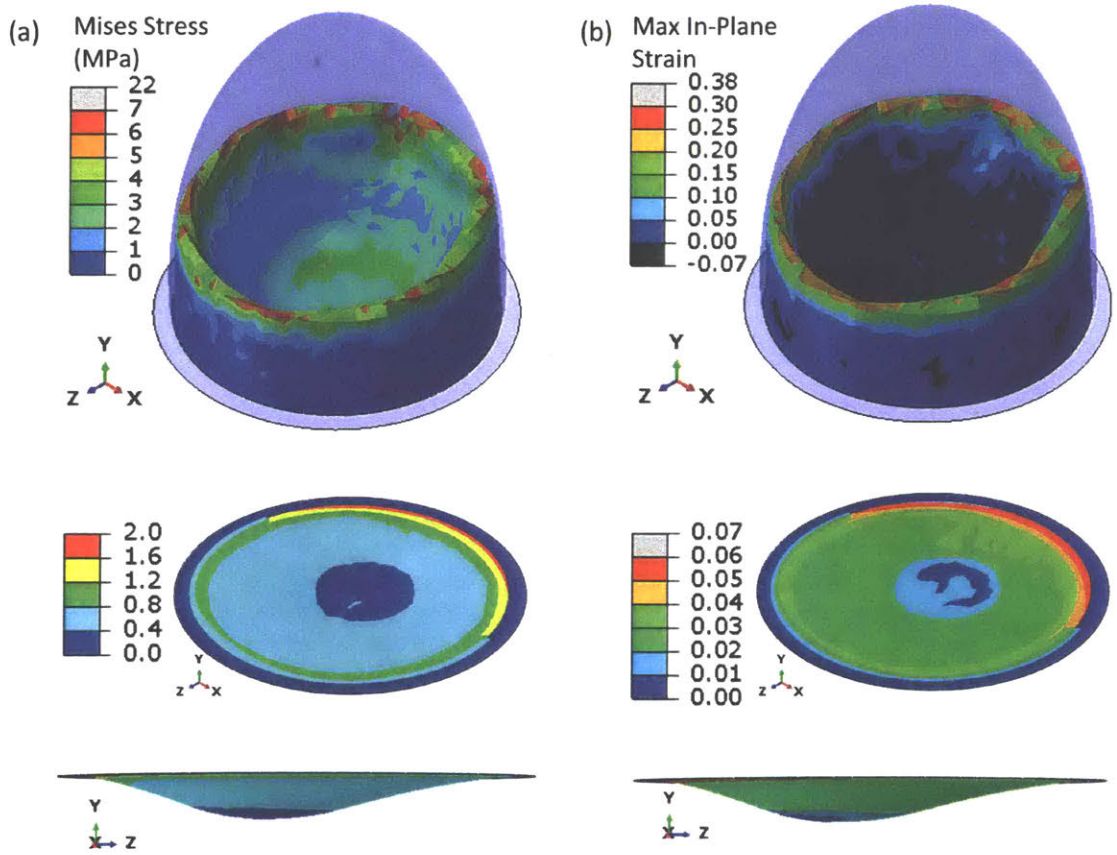

Figure 4-7: Stress and strain predictions. (a) Von Mises stress contour plots for the overall device, and the lower membrane (top-down and side views). (b) Maximum in-plane strain for the overall device, and the lower membrane (top-down and side views).

With the SPH technique, the model predicts the profile of the fluid movement, with the maximum velocity of 17 mm/s when the lower membrane starts to deform. This can be seen in Fig. 4-9.

Using the large deflection circular plate analytical approximation, we were able to predict the deformation in the radial, vertical, and tangential directions along the

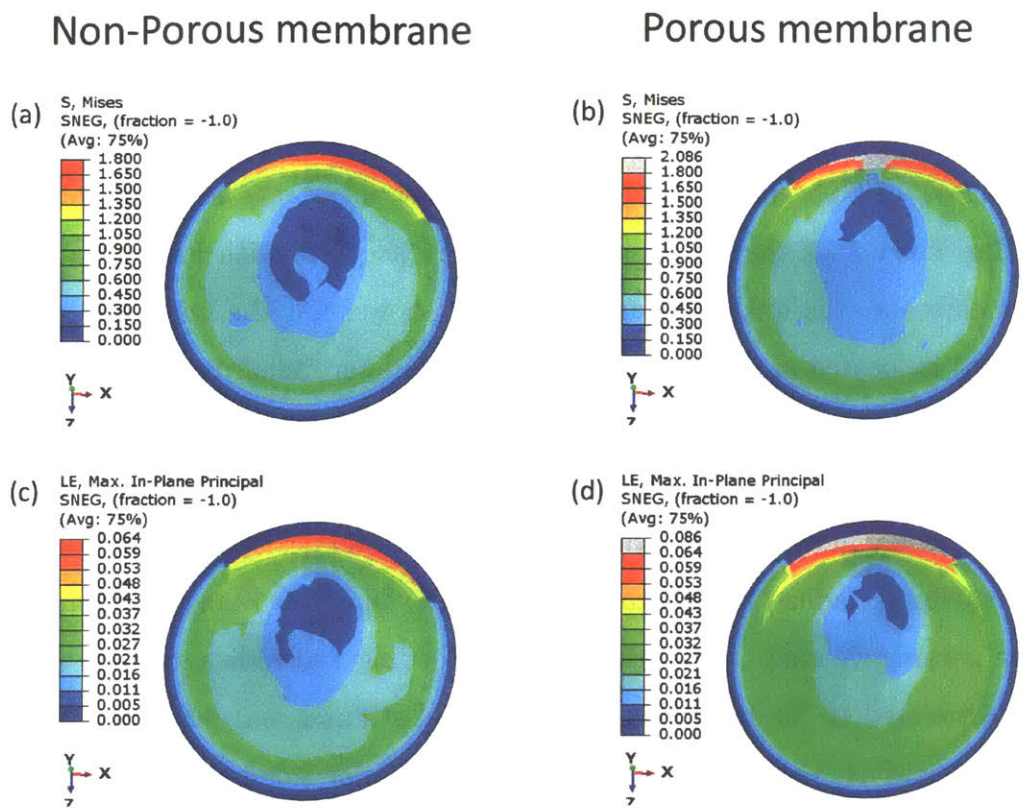

Figure 4-8: Comparison of the FE results for porous and non-porous membrane. (a, b) Von Mises stress prediction of the porous and non-porous membranes (top-down view). (a, b) Maximum in-plane strain of the porous and non-porous membranes (top-down view).

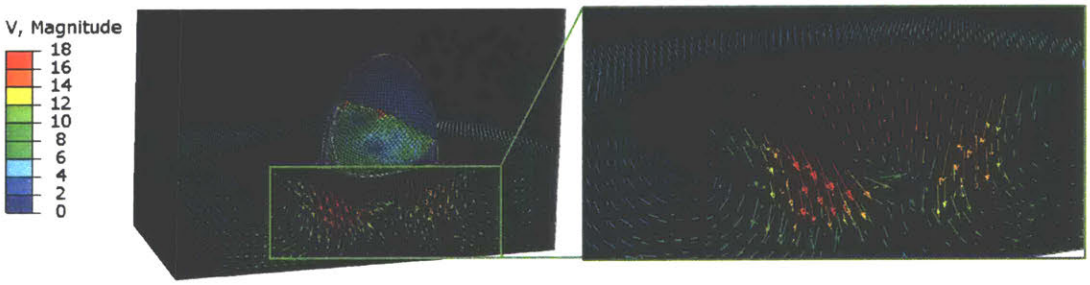

Figure 4-9: Flow prediction by the smooth particle hydrodynamic model. The model showing the direction and magnitude of fluid flow surrounding the fibRobot during actuation

radial distance, see Fig. 4-10. In order to evaluate the performance of this approximation, w and r were nondimensionalized as $W = \frac{w}{h}$, $W_o = \frac{w_o}{h}$, and $\xi = \frac{r}{a}$. W_o is the deflection-thickness ratio, where $W_o < 0.05$ is usually considered small deflection,

and $0.1 < W_o < 10$ is considered large deflection. The analytical approximation was compared with the numerical solution (FEA) using the W vs. ξ plots. Two scenarios were compared, shown in Fig. 4-10(a and b). The former was recreated from Zhang [53] with W_o of 0.95 and the latter was the lower membrane scenario with W_o of 6.1. They show that the approximation is more accurate with lower W_o. For the lower membrane, the analytical approximation shows that the maximum defection (0.46 mm) is located at the center while the maximum radial displacement (0.0013 mm) is not. According to Equation 4.5 and 4.6, the maximum radial strain (near the center), and maximum tangential strain (at the center) have similar magnitude (0.281%) but are in different locations. The radial strain near the center (within 40% of the maximum radius) is close to the maximum value (less than 5% difference).

The parametric study shows that pressure loading and radius size are both positively correlated to the deflection while material stiffness and membrane thickness are both negatively correlated to the deflection. Similar trends are observed for the maximum radial strain and tangential strain, see Fig. 4-11.

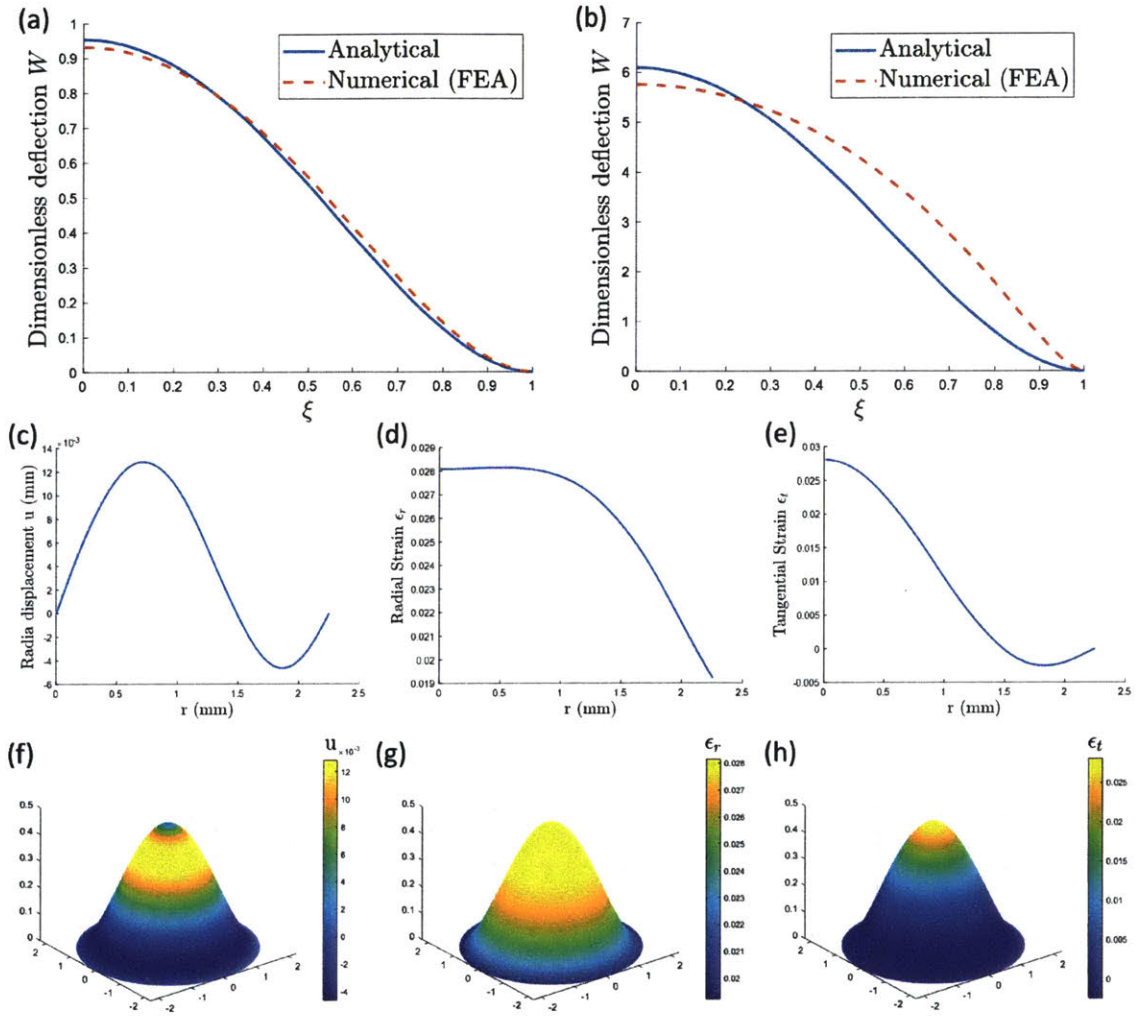

Figure 4-10: Analytical approximations for large deflection circular plates. (a, b) Plots of dimensionless deflection (w) along with dimensionless radius (ξ) to compare the analytical and numerical solutions. The plate parameters a, h, E, q are recreated from Zhang [53] in (a) and are set the same as the lower membrane of fibRobot in (b). (c - e) Plots of radial displacement (u), radial strain (ϵ_r), and tangential strain (ϵ_t) along with radial distance (r) under the lower membrane condition. (f - e) The corresponding contour plots of u, ϵ_r, and ϵ_t.

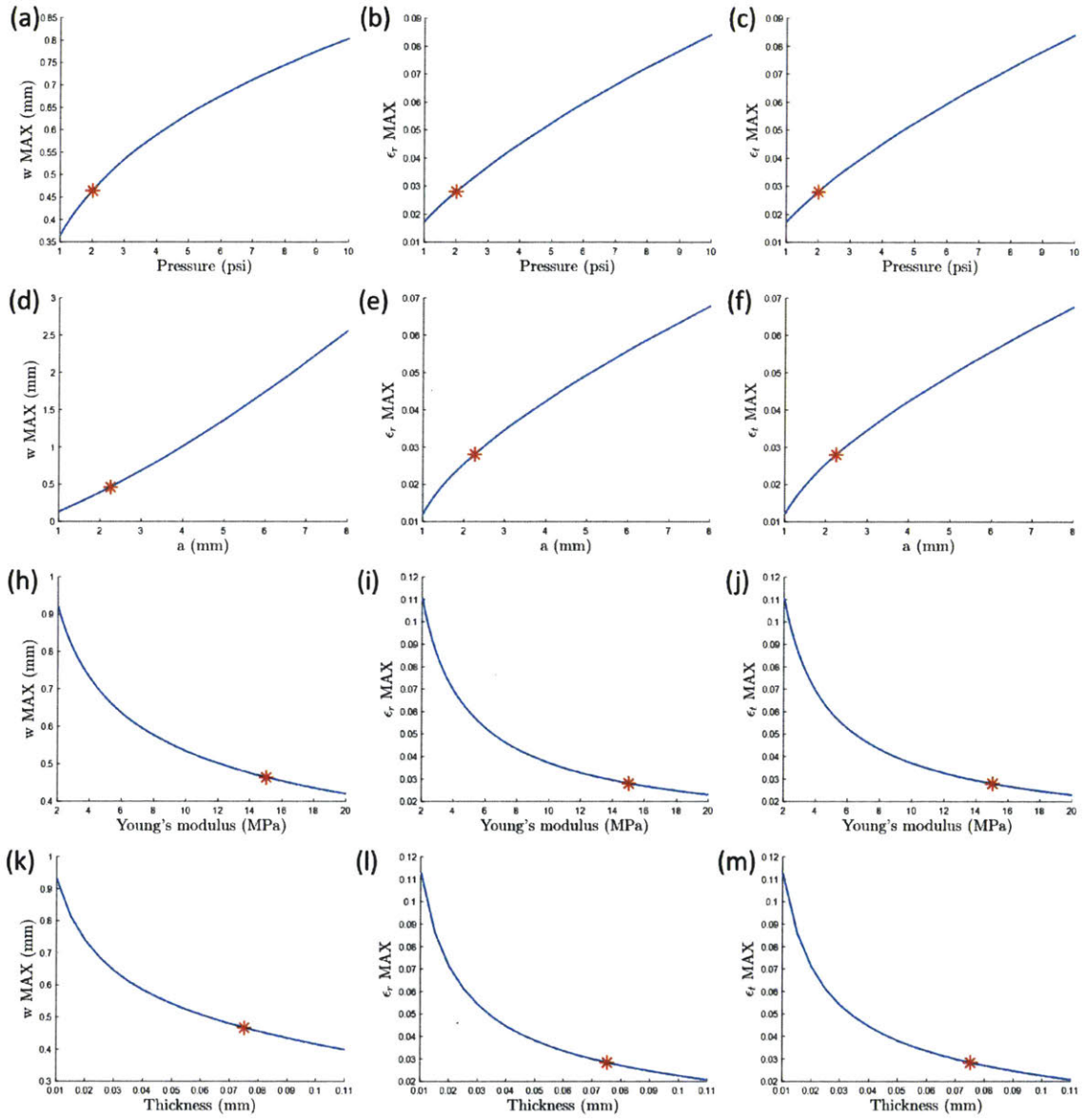

Figure 4-11: Parametric study using large deflection plate analytical approximation. Using the lower membrane scenario (orange star) as the baseline, pressure (a-c), size (d-f), material stiffness (h-j), and membrane thickness (k-m) are tuned showing the effects on w, ϵ_r, and ϵ_t.

4.3 Discussion

In this study, both the FE model and the FSI model have been successfully developed to evaluate the lower membrane strain and its surrounding fluid flows during actuation of the fibRobot. The FE model was validated with experimental measurement of actuation force. A large deflection plate analytical approximation was also implemented to evaluate the effect of a range of design parameters on the membrane strain.

The experimental measurements and computational prediction of actuation force show an excellent agreement, Fig. 4-6. The FE model slightly under-predicted strain at low actuation pressures ($\approx$ 2 psi) and over-predicted at high actuation pressures ($\approx$ 8 psi). One limitation is that the geometry of the FE model is axisymmetric while the results (deformation, stress, and strain fields) are not. This is due to buckling that happens in the middle of the balloon. The solution of buckling is non-unique and therefore the contact between the middle balloon and lower membrane does not have to be in the center. This resulted in the asymmetric fields. Another concern regarding the FE simulation is the choice of the TPU material model. The Ogden 3rd order model had the best curve fitting result because it has higher order terms than the Neo-Hookean and Money-Rivlin model. However, these higher order models are prone to be unstable outside of a certain range of strain, which can be seen in the Yeoh model in Fig. 4-3(c). With an actuation pressure of 2 psi, the maximum strain in the lower membrane, 7%, falls inside the stable range of the Ogden model. However, if design parameters were changed such that the strain increases significantly, a more stable material model should be used.

The SPH model predicted the maximum flow velocity to be 17 mm/s which is much high the interstitial fluid flow without actuation on (up to 0.004 mm/s) [55] but lower than the aortic blood flow (120 cm/s) [56]. This model should be validated experimentally in the future. *In vivo* echocardiogram has been used to validate SPH model of flows in the left ventricle [57]. However, the scale of the fibRobot is much smaller which increases the difficulties of getting the high resolution *in vivo*

measurements. An alternative would be to use Particle Image Velocimetry (PIV) to measure the flow profile in an *ex vivo* setup.

In order to study the effect of strain on the fibrotic response of cells, we will need to test the cells with different range of strains, provided by different designs of the fibRobot. Therefore, a parametric study using computational modeling would be useful to guide the design of the device to achieve a certain desired strain at the lower membrane. Both the FE and FSI models were computationally expensive due to the fact that buckling, contact, and multi-physics interactions are happening in the model. In this study, by using the explicit/dynamic solver, the FE model took about 1.5 hours and the FSI model took about 6 hours with 16 processors. It is not ideal to do parametric studies with these models. Here, we simplified the model to a circular plate and further simplified it to an analytical approximation. As shown in 4-10, the approximation gives a descent prediction on the deformation field. The analytical maximum deflection (0.46 mm) is also comparable to the full FE model prediction (0.38 mm) given that the structure and material model were both simplified in the analytically approximation. The parametric study clearly shows the effect of different design parameters on the maximum strain of the membrane. The original design of the fibRobot provides 7% of the maximum strain which is lower than other studies [58, 59, 60]. According to the parametric study, we could increase the actuation pressure, increase the membrane radius, reduce the thickness, or use a softer material to achieve higher strain.

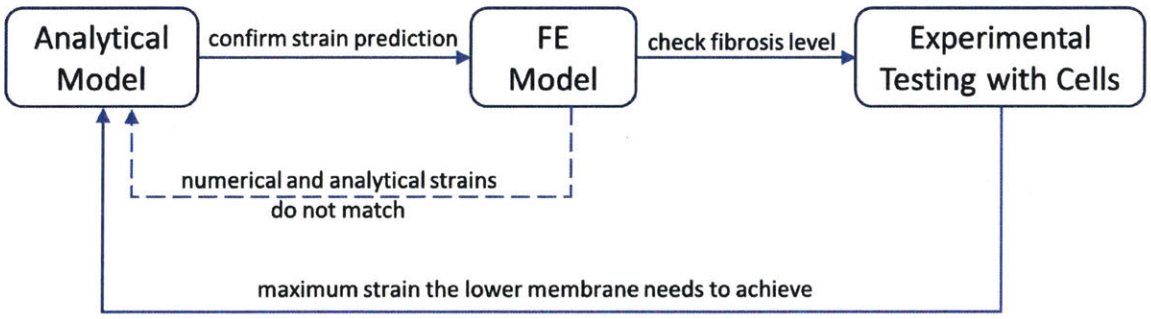

Figure 4-12: Computational modeling assisted optimization work-flow for fibRobot.

As summarized in Chapter 2, finite element analysis can be very powerful on

medical device optimization, especially for mechanical devices [39, 42, 44]. With the simplified geometry of the fibRobot and the analytical model, computational analysis can have a great impact on the optimization process of fibRobot following the proposed work-flow in Fig. 4-12. The iterations between the analytical and FE models can be reduced by improving the accuracy of the analytical approximation, for instance it can incorporate a hyperelastic rather than a linear elastic constitutive model. On the other hand, the fluid-structure interaction model is also very important for the design of the fibRobot especially for the porous-membrane version which can deliver therapies while being actuated. Our *in vivo* study [7] showed that actuation actually improved the drug delivery rate, see Fig. 4-13. To explicitly model the drug transport from the device to the tissue environment can be quite challenging resulting from the facts that (1) the pore diameter (10 micron) is much smaller than the lower membrane diameter; (2) SPH does not support porous media flow. An alternative would be to first use a micro-scale model to measure the flow resistance of the porous membrane and subsequently use it in a macro-scale model to simulate the porous media flow coupling with the structural shell membrane model. This multi-scale fluid-structure model would be much more representative to the drug transport behavior in the fibRobot.

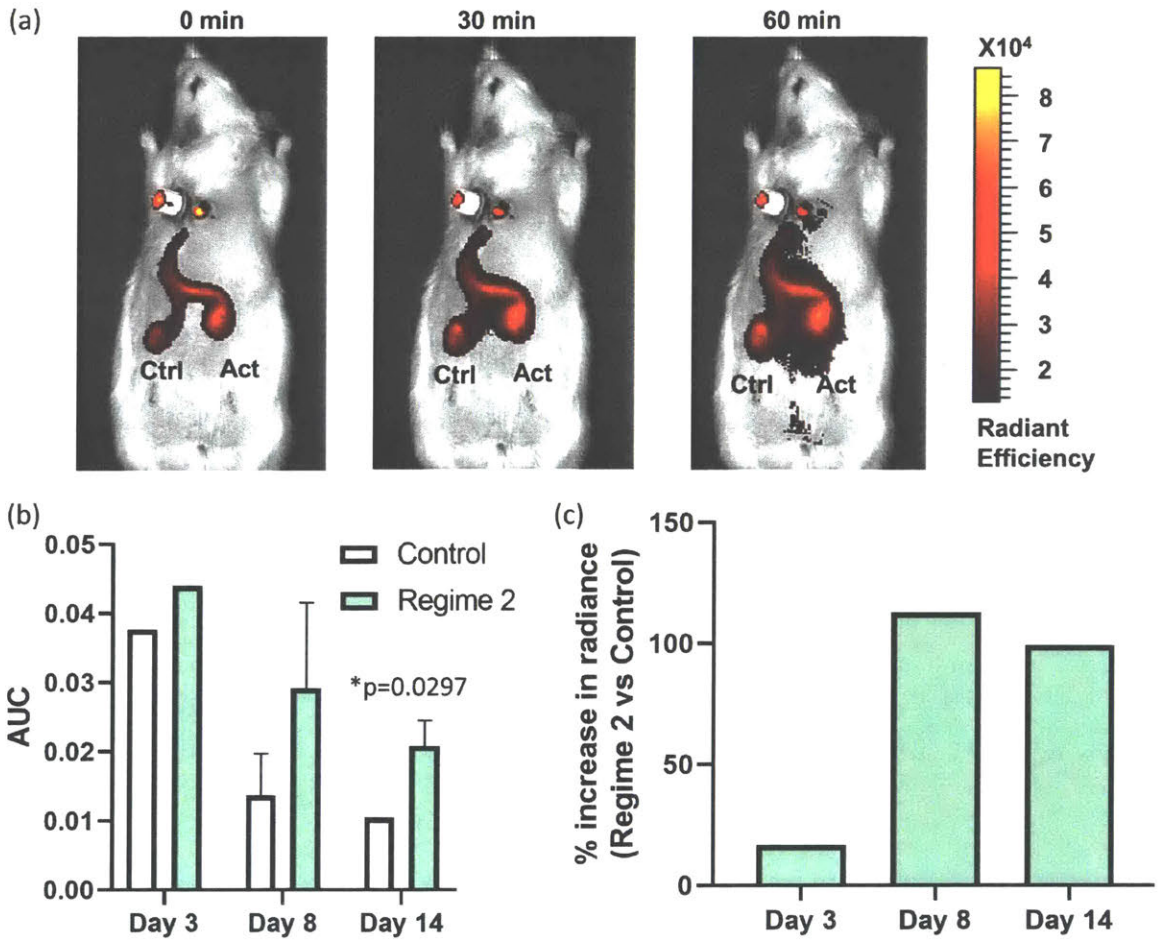

Figure 4-13: Enhanced pharmacokinetics through porous fibRobot with actuation [7]. (a) Images from the *In Vivo* Imaging System (IVIS) at day 14 at 0 minutes, 30 minutes and 60 minutes showing the implanted actuation (regime 2) and control groups. (b) Area under the curve at day 3, 8 and 14 for actuated and control groups n=1-4/group/timepoint, Data are mean ± SD, *p<0.05. (c) Percentage increase of actuation group over control at each timepoint n=1-4/group. Ctrl=control, Act=act, AUC = area under curve.

Chapter 5

Conclusion and Future Work

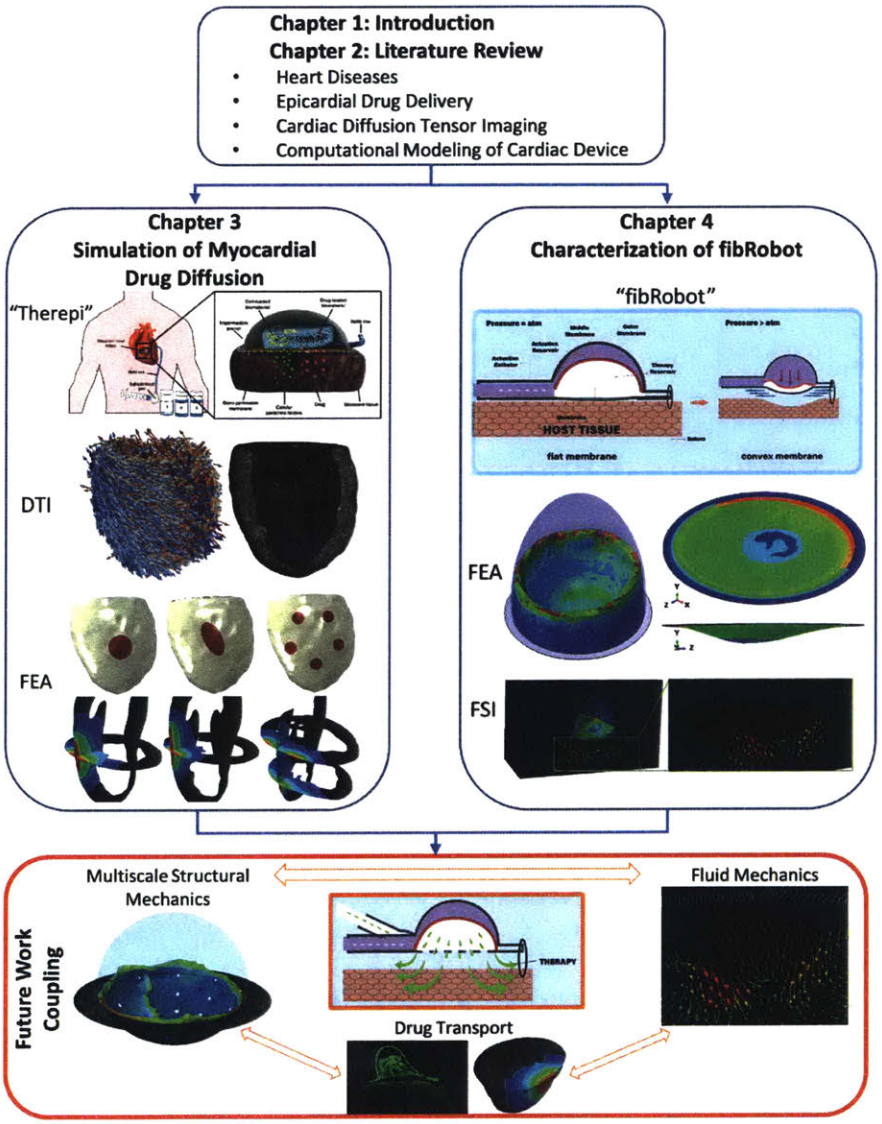

This thesis aimed to use computational modeling to support the design and development of epicardial drug delivery devices. In Chapter 3, we combined finite element simulation with diffusion tensor imaging to characterize the anisotropic diffusion in the myocardium. The validated model was further used to evaluate the performance of different Therepi designs by predicting their diffusion profiles over time. In Chapter 4, we used different modeling techniques, structural mechanics and smooth particle hydrodynamics, to illustrate the mechanical effect and surrounding fluid flow interaction which we hypothesize to interfere with the fibrosis process. We also conducted a parametric study on various design parameters of the fibRobot using an analytical model. This model combined with the high fidelity FE simulation is proposed to be a potential framework to support the planning of future experimental studies and optimize the design of the device.

As discussed in Chapter 3 and 4, there are a few limitations of this study which are listed here. (1) Diffusion coefficients were calculated based on the assumptions of fast diffusion following the fiber direction and minimum detectable concentration were estimated from the T1 relaxation map. These resulted in over prediction of the diffusion lengths in the model. Iterative parameter estimation through an inverse FE model is needed to optimized the diffusion coefficient and therefore provide a better match between the computational prediction and experimental data. (2) Advection and binding of the drug were not considered in the subject-specific LV diffuison model. Combining the three-phrase drug transport model [34] with our anisotropic diffusion model will improve the fidelity of the simulation and therefore derive more useful information to guide the optimization of the device design. (3) As a preliminary study, the velocity prediction from the SPH model needs to be validated with experimental data, preferentially from the particle image velocimetry technique. (4) The analytical approximation under-predicted membrane strains compared to the FE solution due to the simplifications of material model and assumptions of the plate-like deformed shape. Deriving an analytical solution that incorporates a hyperelastic model with a more realistic membrane-like deformed shape would improve the performance of the parametric study and reduce the iteration between the using the analytical solution

and the computational expansive numerical simulation.

With all of the these limitations being addressed, the future work would be to couple multiple physics models (structural mechanics, fluid mechanics and drug transport) that have been described in this thesis to a single simulation as pictured in Fig. 1-1. As mentioned in Chapter 4, the porous membrane version of the fibRobot is capable of mechanical stimulating while delivering therapies. A fully coupled multiphysics model will achieve a much more realistic description of the drug transport process in the fibRobot and therefore give more efficient guidance for design optimization.

In many different industries, computational modeling is a crucial scientific tool that is involved in their daily design and development work-flow to get innovative products [61]. Medical device designers have started to embrace this tool in the past decade [62]. According to this thesis and other previous works discussed in Section 2.4, computational modeling has the potential to reduce, if not replace, the needs of a lot physical experiments, which are expensive and time consuming. Like many of the other previous works, there are some difficulties in actually incorporating the numerical simulations into the iterative design process. First of all, the generation of the FE models is not automatic and therefore manually creating large number of different designs for virtual testing is still very time consuming. Secondly, there are numerous design possibilities and it is not possible to test all of them even through virtual prototyping. Therefore, we need feedback criteria to guide the changes of the computational model. Last but not least, there are a number to assumptions and simplifications applied to the model which affect its accuracy. Essentially, computational modeling is trying to use numerical method to describe the physics happen in the object and predict its behavior. It is difficult, if not impossible, to capture all the physics happening in a device. Thus, in order to make the most benefit out of these modeling techniques, it is important to identify the region of interest and find a balance between accuracy and computational feasibility. With rapid advance of computing technology, such as parallel computing, GPU computing, and cloud storage, the capability of building high fidelity multiphysics fully coupled models will be increased drastically and eventually benefit the design of medical devices.

Appendix A

Diffusion Coefficient Sensitivity Study

Since the diffusivity calculation was based on manually measured diffusion lengths and a 1D diffusion assumption was made while using Fick's second law, various errors could be introduced to the calculation of the diffusivity value. Thus, a sensitivity study was also conducted in order to understand the effect of the anisotropic diffusivity on the predicted concentration profile. As shown in Fig. A-1, a simple rectangle model ($20 \times 20 \times 2.5\ mm^3$) with transmurally varying local orientation, which mimics the cardiac fiber orientation, was created. A circular reservoir interface with radius of 5 mm was created on the "epicardium", where the local orientation is -60° with respect to the top of the rectangle. The temperature boundary condition at the interface was set to be 0.221 K (representing a concentration of 0.1201 M drug analog) and the fiber (D_F) diffusion coefficients was set to $2.778 \times 10^{-14}\ mW/(mm.k)$. The fiber-crossfiber diffusivity ratio (R) was assumed to be the eigenvalue ratio (0.566) calculated from rat heart DTI provided by Teh et al. [23]. As a result, the cross-fiber diffusivity became $1.572 \times 10^{-14}\ mW/(mm.k)$. All these values were calculated from an *ex vivo* study where CT contrast agent phosphomolybdic (PMA) was delivered on a rat heart. The PMA diffusion profile was collected from a μCT100 microCT scanner (Scanco Medical, Wangen-Bruttisellen, Switzerland). The measurements of the diffusion coefficient were calculated following the method described in Chapter 3. With this baseline model, diffusivity ratio (R) was reduced by either decreasing the D_{CF} (Study Set 1) or increasing the DF (Study Set 2), see Table A.1. Results of

each study are shown in Fig. A-2 and Fig. A-3, respectively.

The study shows that (1) transmural diffusion decreases when cross-fiber diffusivity decreases; (2) the anisotropic profile is less discernible in the endocardium and the epicardium due to the transmurally varying fiber orientation;(3) as fiber diffusivity increases, the drug concentration in the center is decreased but the concentration in the border is increased.

These results can be used as a guidance on how to adjust the diffusivity in the fiber and cross-fiber directions so as to have a better match of the predicted diffusion profile with the MRI data.

Table A.1: Sensitivity study sets

Study Sets	Test No.	R	D_F $(mW/(mm.k))$	D_{CF} $(mW/(mm.k))$
Study 1	1	0.566	2.778E-14	1.572E-14
Study 1	2	0.283	2.778E-14	0.786E-14
Study 1	3	0.141	2.778E-14	0.393E-14
Study 2	1	0.566	2.778E-14	1.572E-14
Study 2	4	0.283	5.556E-14	1.572E-14
Study 2	5	0.141	11.11E-14	1.572E-14

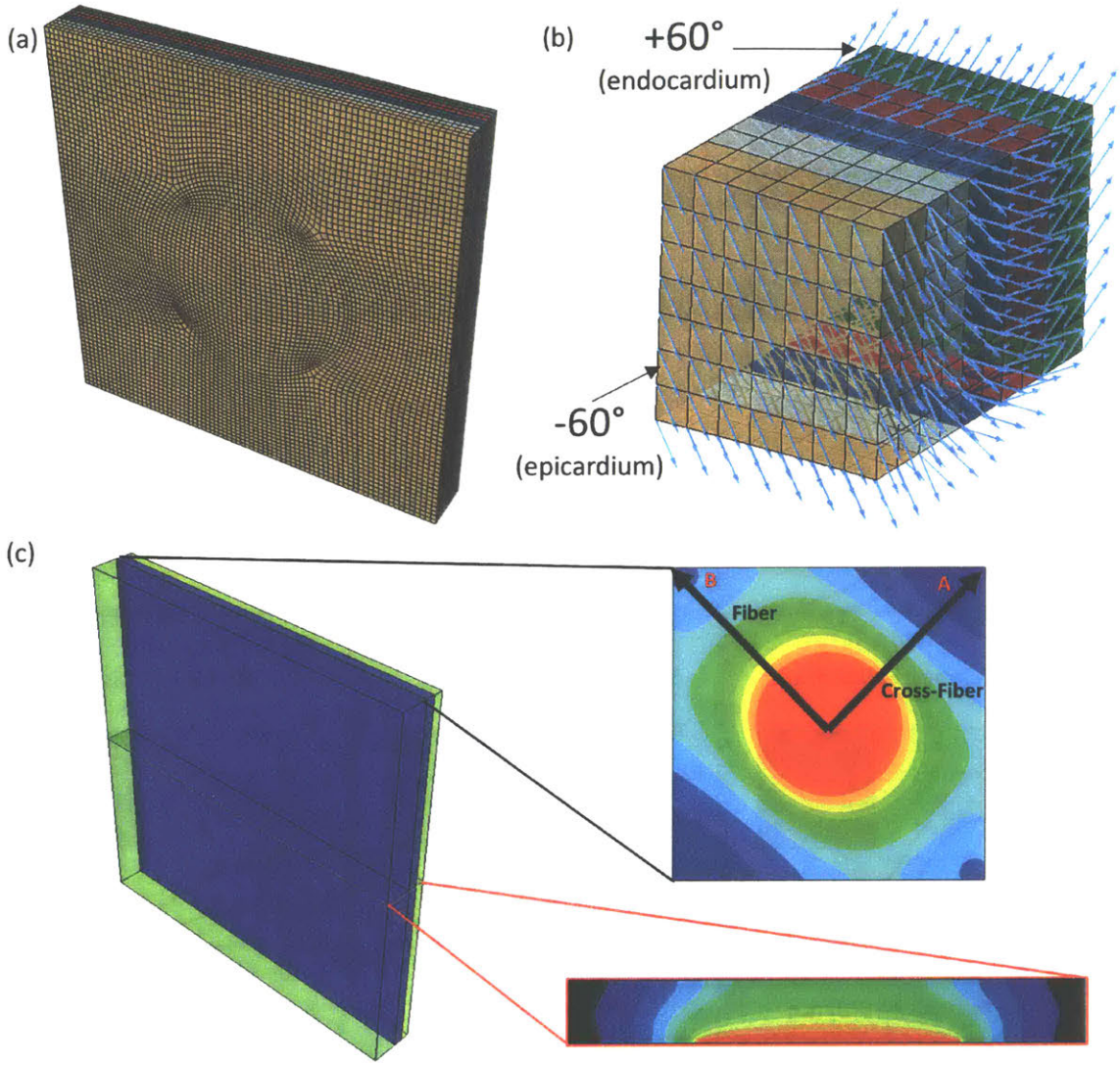

Figure A-1: An overview of the diffusion coefficient sensitivity study. (a) A block with five different layers, each with its own local element orientation mimicking the transmurally varying fiber orientation in the myocardium. (b) The details of the orientation in each layer, varying from -60° (yellow) to 60° (Green), with respect to the top. (c) The results are shown in the second last layer (top right) away from the reservoir and the mid-transmural plane (bottom right).

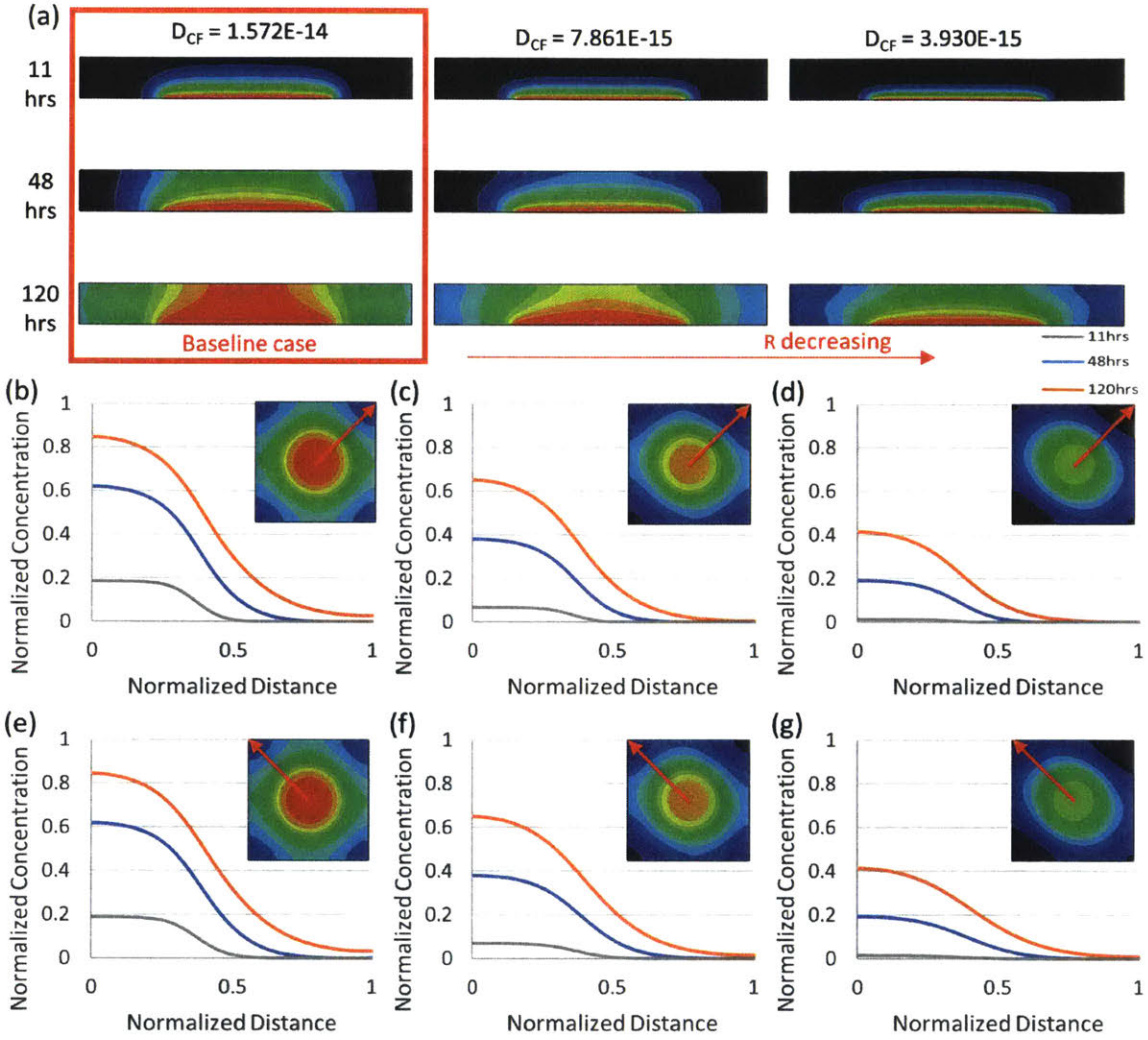

Figure A-2: Concentration predictions of study 1. (a) Concentration contour plots on the mid-transmural plane at 11, 48 and 120 hours. From the left to right columns are Test 1, 2, and 3 as per Table A.1. (b - d) Path plots of concentration along the cross-fiber direction on the second last layer. The counter plot on that layer at 120 hours are also shown in the sub-figure with red arrow indicating the path plot direction. (e - g) Similar path plots but along the fiber direction. D_{CF} = diffusion coefficient in the cross-fiber direction.

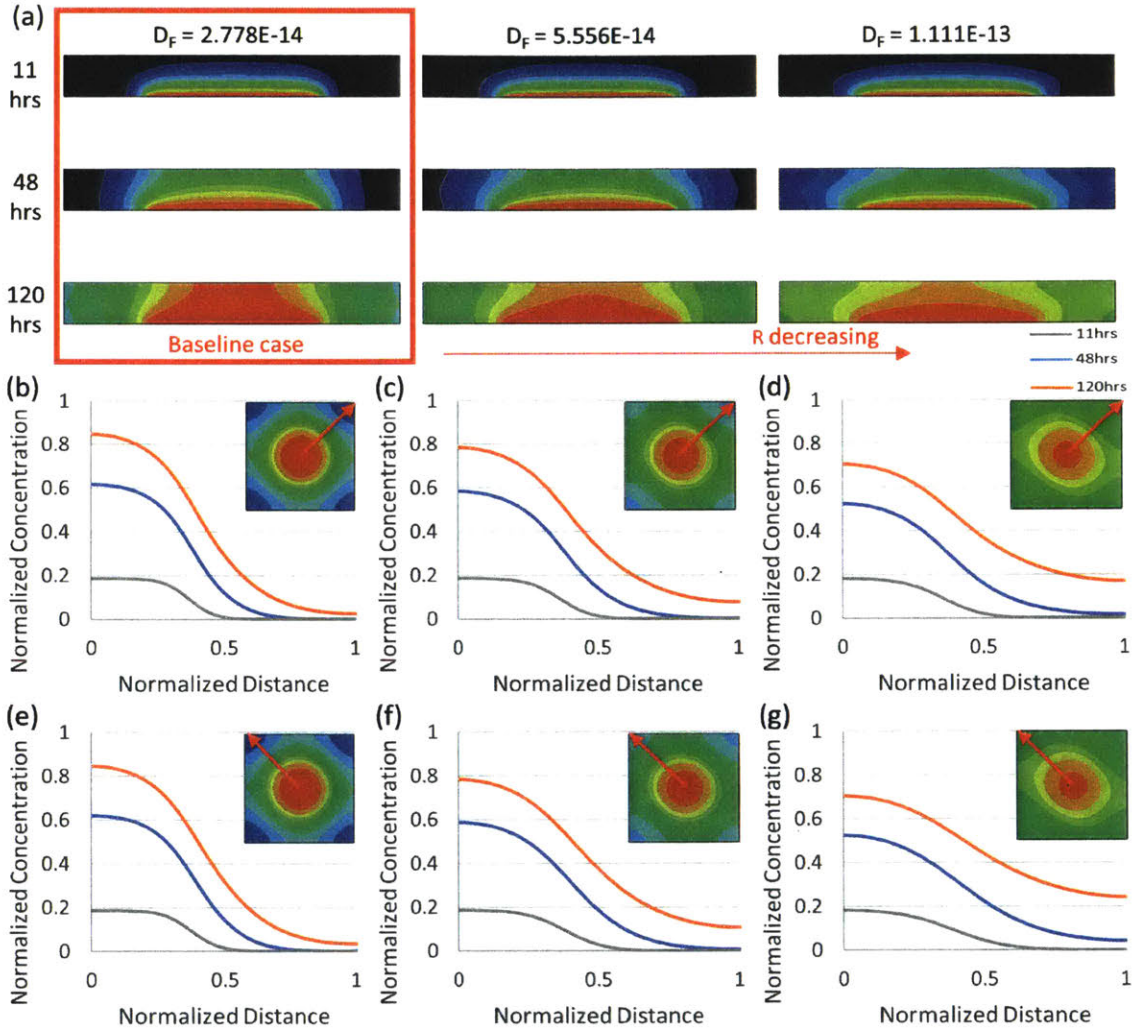

Figure A-3: Concentration predictions of study 2. (a) Concentration contour plots on the mid-transmural plane at 11, 48 and 120 hours. From the left to right columns are Test 1, 4, and 5 as per Table A.1. (b - d) Path plots of concentration along the cross-fiber direction on the second last layer. The counter plot on that layer at 120 hours are also shown in the sub-figure with red arrow indicating the path plot direction. (e - g) Similar path plots but along the fiber direction. D_F = diffusion coefficient in the fiber direction

Bibliography

[1] Bill Cannon. Cardiovascular disease: Biochemistry to behaviour. *Nature*, 493(7434):S2–S3, 2013.

[2] National Center for Health Statistics. Table 19. Leading causes of death and numbers of deaths, by sex, race, and Hispanic origin: United States, 1980 and 2016. Technical report, NCHS, 2017.

[3] Mikhail Y. Maslov, Elazer R. Edelman, Matthew J. Pezone, Abraham E. Wei, Matthew G. Wakim, Michael R. Murray, Hisashi Tsukada, Iraklis S. Gerogiannis, Adam Groothuis, and Mark A. Lovich. Myocardial drug distribution generated from local epicardial application: Potential impact of cardiac capillary perfusion in a swine model using epinephrine. *Journal of Controlled Release*, 194:257–265, 11 2014.

[4] Jose R. Garcia, Peter F. Campbell, Gautam Kumar, Jonathan J. Langberg, Liliana Cesar, Lanfang Wang, Andrés J. García, and Rebecca D. Levit. A Minimally Invasive, Translational Method to Deliver Hydrogels to the Heart Through the Pericardial Space. *JACC: Basic to Translational Science*, 2(5):601–609, 10 2017.

[5] Takeyoshi Ota, Nicholas A. Patronik, David Schwartzman, Cameron N. Riviere, and Marco A. Zenati. Minimally invasive epicardial injections using a novel semiautonomous robotic device. *Circulation*, 118(14 Suppl), 2008.

[6] William Whyte, Ellen T. Roche, Claudia E. Varela, Keegan Mendez, Shahrin Islam, Hugh O'Neill, Fiona Weafer, Reyhaneh Neghabat Shirazi, James C. Weaver, Nikolay V. Vasilyev, Peter E. McHugh, Bruce Murphy, Garry P. Duffy, Conor J. Walsh, and David J. Mooney. Sustained release of targeted cardiac therapy with a replenishable implanted epicardial reservoir. *Nature Biomedical Engineering*, 2(6):416–428, 6 2018.

[7] E.B. Dolan, C.E. Varela, K. Mendez, W. Whyte, R.E. Levey, S.T. Robinson, S.E. Rothenbucher, E. Maye, Y. Fan, R. Wylie, M. Monaghan, P. Dockery, G.P. Duffy, and E.T. Roche. An actuatable soft reservoir modulates host foreign body response. *Under Review*, 2019.

[8] Mikhail Maslov, Stephan Foianini, and Mark Lovich. Delivery of drugs, growth factors, genes and stem cells via intrapericardial, epicardial and intramyocardial routes for sustained local targeted therapy of myocardial disease, 2017.

[9] Yoshinori Miyahara, Noritoshi Nagaya, Masaharu Kataoka, Bobby Yanagawa, Koichi Tanaka, Hiroyuki Hao, Kozo Ishino, Hideyuki Ishida, Tatsuya Shimizu, Kenji Kangawa, Shunji Sano, Teruo Okano, Soichiro Kitamura, and Hidezo Mori. Monolayered mesenchymal stem cells repair scarred myocardium after myocardial infarction. *Nature Medicine*, 12(4):459–465, 4 2006.

[10] Kha N. Le, Chao Wei Hwang, A. Rami Tzafriri, Mark A. Lovich, Alison Hayward, and Elazer R. Edelman. Vascular regeneration by local growth factor release is self-limited by microvascular clearance. *Circulation*, 119(22):2928–2935, 2009.

[11] Kaytlyn A. Gerbin, Xiulan Yang, Charles E. Murry, and Kareen L.K. Coulombe. Enhanced electrical integration of engineered human myocardium via intramyocardial versus epicardial delivery in infarcted rat hearts. *PLoS ONE*, 10(7), 2015.

[12] Vinod Labhasetwar, Alan Kadish, Thomas Underwood, Matthew Sirinek, and Robert J. Levy. The efficacy of controlled release D-sotalol-polyurethane epicardial implants for ventricular arrhythmias due to acute ischemia in dogs. *Journal of Controlled Release*, 23(1):75–85, 1 1993.

[13] Vinod Labhasetwar, Tom Underwood, Marsha Gallagher, Gina Murphy, Jonathan Langberg, and Robert J. Levy. Sotalol Controlled-Release Systems for Arrhythmias: In Vitro Characterization, in Vivo Drug Disposition, and Electrophysiologic Effects. *Journal of Pharmaceutical Sciences*, 83(2):156–164, 2 1994.

[14] Rivka Siden, William E. Flowers, and Robert J. Levy. Epicardial propranolol administration for ventricular arrhythmias in dogs: matrix formulation and characterization. *Biomaterials*, 13(11):764–770, 1 1992.

[15] Robert W. Bolderman, J.J. Rob Hermans, Leonard M. Rademakers, Monique M.J. de Jong, Peter Bruin, Aylvin A. Dias, Frederik H. van der Veen, and Jos G. Maessen. Epicardial application of an amiodarone-releasing hydrogel to suppress atrial tachyarrhythmias. *International Journal of Cardiology*, 149(3):341–346, 6 2011.

[16] Mikhail Y. Maslov, Elazer R. Edelman, Abraham E. Wei, Matthew J. Pezone, and Mark A. Lovich. High concentrations of drug in target tissues following local controlled release are utilized for both drug distribution and biologic effect: An example with epicardial inotropic drug delivery. *Journal of Controlled Release*, 171(2):201–207, 2013.

[17] Justin D. Pearlman, Mark G. Hibberd, Michael L. Chuang, Kazumasa Harada, John J. Lopez, Stephen R. Gladstone, Menahem Friedman, Frank W. Sellke, and Michael Simons. Magnetic resonance mapping demonstrates benefits of VEGF-induced myocardial angiogenesis. *Nature Medicine*, 1(10):1085–1089, 10 1995.

[18] D Ladage, I. C. Turnbull, K Ishikawa, Y Takewa, K Rapti, C Morel, I Karakikes, L Hadri, J Müller-Ehmsen, K. D. Costa, R. J. Hajjar, and Y Kawase. Delivery of gelfoam-enabled cells and vectors into the pericardial space using a percutaneous approach in a porcine model. *Gene Therapy*, 18(10):979–985, 2011.

[19] Gang Wang, Wenhua Li, Waqas Nawaz, Xiaoqian Liao, Meng-Qi Yang, Li Zhang, Farhan-Ullah Khan, Xiaoming Qi, Dingding Chen, Zhijie Wang, Feng Yu, Lei Han, and Xiaohui Zhou. Efficacy of a Novel Epicardium Drug Delivery System for Bone Marrow Stem Cells Treating Heart Failure After Myocardial Infarction. *Insights in Stem Cells*, 2(2), 12 2016.

[20] Ellen T Roche, Markus A Horvath, Isaac Wamala, Ali Alazmani, Sang-Eun Song, William Whyte, Zurab Machaidze, Christopher J Payne, James C Weaver, Gregory Fishbein, Joseph Kuebler, Nikolay V Vasilyev, David J Mooney, Frank A Pigula, and Conor J Walsh. Soft robotic sleeve supports heart function. *Science Translational Medicine*, 9(373), 2017.

[21] Patric Hagmann, Lisa Jonasson, Philippe Maeder, Jean-Philippe Thiran, Van J Wedeen, and Reto Meuli. Understanding diffusion MR imaging techniques: from scalar diffusion-weighted imaging to diffusion tensor imaging and beyond. *Radiographics : a review publication of the Radiological Society of North America, Inc*, 26 Suppl 1:205–23, 2006.

[22] E W Hsu, A L Muzikant, S A Matulevicius, R C Penland, and C S Henriquez. Magnetic resonance myocardial fiber-orientation mapping with direct histological correlation. Technical Report 5 Pt 2, MIT, 1998.

[23] Irvin Teh, Darryl McClymont, Rebecca A. B. Burton, Mahon L. Maguire, Hannah J. Whittington, Craig A. Lygate, Peter Kohl, and Jürgen E. Schneider. Resolving Fine Cardiac Structures in Rats with High-Resolution Diffusion Tensor Imaging. *Scientific Reports*, 6(1):30573, 2016.

[24] Sonia Nielles-Vallespin, Zohya Khalique, Pedro F. Ferreira, Ranil de Silva, Andrew D. Scott, Philip Kilner, Laura Ann McGill, Archontis Giannakidis, Peter D. Gatehouse, Daniel Ennis, Eric Aliotta, Majid Al-Khalil, Peter Kellman, Dumitru Mazilu, Robert S. Balaban, David N. Firmin, Andrew E. Arai, and Dudley J. Pennell. Assessment of Myocardial Microstructural Dynamics by In Vivo Diffusion Tensor Cardiac Magnetic Resonance. *Journal of the American College of Cardiology*, 69(6):661–676, 2017.

[25] Tina M. Morrison. Reporting of Computational Modeling Studies in Medical Device Submissions - Draft Guidance for Industry and Food and Drug Administration Staff. Technical Report 301, FDA Center for Devices and Radiological Health, 2014.

[26] C.A. Sweeney, P.E. McHugh, J.P. McGarry, and S.B. Leen. Micromechanical methodology for fatigue in cardiovascular stents. *International Journal of Fatigue*, 44:202–216, 11 2012.

[27] Harry A Dwyer, Peter B Matthews, Ali Azadani, Nicolas Jaussaud, Liang Ge, T Sloane Guy, and Elaine E Tseng. Computational fluid dynamics simulation of transcatheter aortic valve degeneration. *Interactive CardioVascular and Thoracic Surgery*, 9(2):301–308, 2009.

[28] Jeffrey M Gardiner, Jingchun Wu, Myounggyu D Noh, James F Antaki, Trevor A Snyder, David B. Paden, and Brad E Paden. Thermal analysis of the PediaFlow pediatric ventricular assist device. *ASAIO Journal*, 53(1):65–73, 2007.

[29] Wenbin Mao, Kewei Li, and Wei Sun. Fluid-Structure Interaction Study of Transcatheter Aortic Valve Dynamics Using Smoothed Particle Hydrodynamics. *Cardiovascular engineering and technology*, 7(4):374–388, 2016.

[30] Adityo Prakosa, Hermenegild J. Arevalo, Dongdong Deng, Patrick M. Boyle, Plamen P. Nikolov, Hiroshi Ashikaga, Joshua J.E. Blauer, Elyar Ghafoori, Carolyn J. Park, Robert C. Blake, Frederick T. Han, Rob S. MacLeod, Henry R. Halperin, David J. Callans, Ravi Ranjan, Jonathan Chrispin, Saman Nazarian, and Natalia A. Trayanova. Personalized virtual-heart technology for guiding the ablation of infarct-related ventricular tachycardia. *Nature Biomedical Engineering*, 2(10):732–740, 10 2018.

[31] D. R. Hose, A. J. Narracott, B. Griffiths, S. Mahmood, J. Gunn, D. Sweeney, and P. V. Lawford. A thermal analogy for modelling drug elution from cardiovascular stents. *Computer Methods in Biomechanics and Biomedical Engineering*, 7(5):257–264, 2004.

[32] F Migliavacca, F Gervaso, M Prosi, P Zunino, S Minisini, L Formaggia, and G Dubini. Expansion and drug elution model of a coronary stent. *Computer Methods in Biomechanics and Biomedical Engineering*, 10(1):63–73, 2007.

[33] Marc Horner, S. Joshi, V. Dhruva, S. Sett, and S. F. C. Stewart. A Two-Species Drug Delivery Model is Required to Predict Deposition from Drug-Eluting Stents. *Cardiovascular Engineering and Technology*, 1(3):225–234, 9 2010.

[34] Akash Pradip Mandal and Prashanta Kumar Mandal. Computational Modelling of Three-phase Stent-based Delivery. *Journal of Exploratory Research in Pharmacology*, 2(2):31–40, 5 2017.

[35] P Zunino, C. D'Angelo, L Petrini, C Vergara, C Capelli, and F Migliavacca. Numerical simulation of drug eluting coronary stents: Mechanics, fluid dynamics and drug release. *Computer Methods in Applied Mechanics and Engineering*, 198(45-46):3633–3644, 2009.

[36] Mokhtarzadeh H, Aw M.S, Khalid K.a, Gulati K, Atkins G.J, Findlay M.D, D Losic, and Peter Pivonka. Computational and experimental model of nano-engineered drug delivery system for trabecular. *11th World Congress on Computational Mechanics (WCCM XI)*, (Wccm Xi):1–12, 2014.

[37] M.A. Khanday and Aasma Rafiq. Variational finite element method to study the absorption rate of drug at various compartments through transdermal drug delivery system. *Alexandria Journal of Medicine*, 51(3):219–223, 9 2015.

[38] Choon-Sik Jhun, Jonathan F Wenk, Zhihong Zhang, Samuel T Wall, Kay Sun, Hani N Sabbah, Mark B Ratcliffe, and Julius M Guccione. Effect of adjustable passive constraint on the failing left ventricle: a finite-element model study. *The Annals of thoracic surgery*, 89(1):132–7, 1 2010.

[39] Jonathan F Wenk, Liang Ge, Zhihong Zhang, Dimitri Mojsejenko, D Dean Potter, Elaine E Tseng, Julius M Guccione, and Mark B Ratcliffe. Biventricular finite element modeling of the Acorn CorCap Cardiac Support Device on a failing heart. *The Annals of thoracic surgery*, 95(6):2022–7, 6 2013.

[40] Kay Sun, Zhihong Zhang, Takamaro Suzuki, Jonathan F Wenk, Nielen Stander, Daniel R Einstein, David A Saloner, Arthur W Wallace, Julius M Guccione, and Mark B Ratcliffe. Dor procedure for dyskinetic anteroapical myocardial infarction fails to improve contractility in the border zone. *The Journal of thoracic and cardiovascular surgery*, 140(1):233–9, 7 2010.

[41] Joe Luis Pantoja, Zhihong Zhang, Mehrzad Tartibi, Kay Sun, Warrick Macmillan, Julius M Guccione, Liang Ge, and Mark B Ratcliffe. Residual Stress Impairs Pump Function After Surgical Ventricular Remodeling: A Finite Element Analysis. *The Annals of thoracic surgery*, 100(6):2198–205, 12 2015.

[42] Richard Carrick, Liang Ge, Lik Chuan Lee, Zhihong Zhang, Rakesh Mishra, Leon Axel, Julius M Guccione, Eugene A Grossi, and Mark B Ratcliffe. Patient-specific finite element-based analysis of ventricular myofiber stress after Coapsys: importance of residual stress. *The Annals of thoracic surgery*, 93(6):1964–71, 6 2012.

[43] Jinkyung Park, Suji Choi, Ajit H Janardhan, Se-Yeon Lee, Samarth Raut, Joao Soares, Kwangsoo Shin, Shixuan Yang, Chungkeun Lee, Ki-Woon Kang, Hye Rim Cho, Seok Joo Kim, Pilseon Seo, Wonji Hyun, Sungmook Jung, Hye-Jeong Lee, Nohyun Lee, Seung Hong Choi, Michael Sacks, Nanshu Lu, Mark E Josephson, Taeghwan Hyeon, Dae-Hyeong Kim, and Hye Jin Hwang. Electromechanical cardioplasty using a wrapped elasto-conductive epicardial mesh. *Science translational medicine*, 8(344):344ra86, 6 2016.

[44] Kevin L. Sack, Brian Baillargeon, Gabriel Acevedo-Bolton, Martin Genet, Nuno Rebelo, Ellen Kuhl, Liviu Klein, Georg M. Weiselthaler, Daniel Burkhoff, Thomas Franz, and Julius M. Guccione. Partial LVAD restores ventricular outputs and normalizes LV but not RV stress distributions in the acutely failing heart in silico. *International Journal of Artificial Organs*, 2016.

[45] Dassault Systèmes. ABAQUS 2018 Documentation, 2018.

[46] Yiling Fan, William Ronan, Irvin Teh, Jurgen E. Schneider, Claudia E. Varela, William Whyte, Peter McHugh, Sean Leen, and Ellen Roche. A comparison of two quasi-static computational models for assessment of intra-myocardial injection as a therapeutic strategy for heart failure. *International Journal for Numerical Methods in Biomedical Engineering*, page e3213, 5 2019.

[47] Martin Genet, Lik Chuan Lee, Ellen Kuhl, and Julius Guccione. Abaqus / Standard - based quantification of human cardiac mechanical properties. *SIMULIA Community Conference*, pages 1–14, 2014.

[48] Martin Genet, Lik Chuan Lee, Rebecca Nguyen, Henrik Haraldsson, Gabriel Acevedo-Bolton, Zhihong Zhang, Liang Ge, Karen Ordovas, Sebastian Kozerke, and Julius M Guccione. Distribution of normal human left ventricular myofiber stress at end diastole and end systole: a target for in silico design of heart failure treatments. *J Appl Physiol*, 117:142–152, 2014.

[49] R F Janz and A F Grimm. Finite-element model for the mechanical behavior of the left ventricle. Prediction of deformation in the potassium-arrested rat heart. *Circulation research*, 30(2):244–52, 2 1972.

[50] John D Gleason, Khanh P Nguyen, Kraig V Kissinger, Warren J Manning, and Richard L Verrier. Myocardial drug distribution pattern following intrapericardial delivery: An MRI analysis. *Journal of Cardiovascular Magnetic Resonance*, 4(3):311–316, 2002.

[51] Yuanyuan Zheng, Hong Zhang, Yuping Hu, Lu Bai, and Jingyi Xue. MnO nanoparticles with potential application in magnetic resonance imaging and drug delivery for myocardial infarction. *International journal of nanomedicine*, 13:6177–6188, 2018.

[52] Rohan D. A. Alvares, Daniel A. Szulc, and Hai-Ling M. Cheng. A scale to measure MRI contrast agent sensitivity. *Scientific Reports*, 7(1):15493, 12 2017.

[53] Yin Zhang. Large deflection of clamped circular plate and accuracy of its approximate analytical solutions. *Science China: Physics, Mechanics and Astronomy*, 59(2):1–11, 2016.

[54] S. Timoshenko; S. Woinowsky-Krieger. *Theory of Plates and Shells*. New York, 2nd edition, 1959.

[55] William J Polacheck, Joseph L Charest, and Roger D Kamm. Interstitial flow influences direction of tumor cell migration through competing mechanisms. *Proceedings of the National Academy of Sciences of the United States of America*, 108(27):11115–20, 7 2011.

[56] Inga Voges, Michael Jerosch-Herold, Jürgen Hedderich, Eileen Pardun, Christopher Hart, Dominik Daniel Gabbert, Jan Hinnerk Hansen, Colin Petko, Hans Heiner Kramer, and Carsten Rickers. Normal values of aortic dimensions,

distensibility, and pulse wave velocity in children and young adults: A cross-sectional study. *Journal of Cardiovascular Magnetic Resonance*, 14(1):77, 11 2012.

[57] Wenbin Mao, Andrés Caballero, Raymond McKay, Charles Primiano, and Wei Sun. Fully-coupled fluid-structure interaction simulation of the aortic and mitral valves in a realistic 3D left ventricle model. *PLOS ONE*, 12(9):e0184729, 9 2017.

[58] Virginia Ballotta, Anita Driessen-Mol, Carlijn V.C. Bouten, and Frank P.T. Baaijens. Strain-dependent modulation of macrophage polarization within scaffolds. *Biomaterials*, 35(18):4919–4928, 6 2014.

[59] Loren A. Matheson, N. Jack Fairbank, Geoffrey N. Maksym, J. Paul Santerre, and Rosalind S. Labow. Characterization of the Flexcell Uniflex cyclic strain culture system with U937 macrophage-like cells. *Biomaterials*, 27(2):226–233, 1 2006.

[60] Loren A. Matheson, Geoffrey N. Maksym, J. Paul Santerre, and Rosalind S. Labow. Cyclic biaxial strain affects U937 macrophage-like morphology and enzymatic activities. *Journal of Biomedical Materials Research Part A*, 76A(1):52–62, 1 2006.

[61] Loren Miller. Product innovation through computational prototypes and supercomputing. *Computing in Science and Engineering*, 19(6):9–17, 11 2017.

[62] Tina M Morrison, Pras Pathmanathan, Mariam Adwan, and Edward Margerrison. Advancing Regulatory Science With Computational Modeling for Medical Devices at the FDA's Office of Science and Engineering Laboratories. *Frontiers in medicine*, 5:241, 2018.